Chemical Geology 662 (2024) 122247

Contents lists available at ScienceDirect

Chemical Geology

journal homepage: www.elsevier.com/locate/chemgeo

The spatial–temporal evolution of Neotethyan subduction in central to Southeast Iran: Constraints from geochemistry, zircon U–Pb–Hf, and Sr–Nd–Pb isotopes

Shahrouz Babazadeh [a,*], Davood Raeisi [b], M. Santosh [c,d], Tanya Furman [e], Sung Hi Choi [f], Massimo D'Antonio [g,*]

[a] Natural Science Research Institute, Chungnam National University, Daejeon 34134, South Korea
[b] School of Geology, College of Science, University of Tehran, Tehran, Iran
[c] School of Earth Sciences and Resources, China University of Geosciences Beijing, Beijing 100083, PR China
[d] School of Physics, Chemistry and Earth Sciences, University of Adelaide, Adelaide, SA 5005, Australia
[e] Department of Geosciences, Pennsylvania State University, University Park, PA 16802, USA
[f] Department of Geological Sciences, Chungnam National University, Daejeon 34134, South Korea
[g] Dipartimento di Scienze della Terra, dell'Ambiente e delle Risorse - DiSTAR, University Federico II, I-80126 Naples, Italy

ARTICLE INFO

Editor: Dr. S Aulbach

Original content: The spatial–temporal evolution of Neotethyan subduction in central to southeast Iran: Constraints from geochemistry, zircon U–Pb–Hf, and Sr–Nd–Pb isotopes (Original data)

Keywords:
Urumieh–Dokhtar magmatic arc
Late Mesozoic–Cenozoic
Flare-up
Sr–Nd–Pb-isotopes
Rollback
Break-off
Diachronous collision

ABSTRACT

Igneous rocks in central Iran preserve proof of several episodes of Late Mesozoic–Cenozoic Neotethyan subduction, and record temporal and spatial variations from subduction to collisional geodynamic regimes that remain a subject of debate. We revisit magmatic rocks from the central Urumieh–Dokhtar magmatic arc (UDMA; 32° 30′ N to 36° 00′ N) and report new major and trace element analyses, whole-rock Sr–Nd–Pb-isotopic data and zircon U–Pb–Hf ages on plutonic rocks from the Kajan region. The data reveal magmatic pulses between 32 and 22 Ma that are represented by igneous rocks with geochemical and isotopic features resulting from melting of a metasomatized, enriched mantle. Modeling indicates the samples represent a mixture of 97% batch melt (from a source with 98.5% mantle melt +1.5% terrigenous sediment) with 3% upper continental crust. The oldest yielded age (*i.e.,* 32 Ma) rules out a lull in magmatism in the central UDMA between 37 and 26 Ma and speaks against distinct flare-up magmatic episodes at ~54–37 Ma and ~ 20–5 Ma in the frontal arc. We hypothesize that magmatism records down-going slab tearing into two pieces beneath the central to SE UDMA, which then changes the geometry and buoyancy of subducting Neotethyan lithosphere. The down-going slab remained involved in central UDMA (*i.e.,* rollback) during Early Miocene whilst arc retreat beneath the SE UDMA proceeded with detachment of subducted oceanic lithosphere (*i.e.,* break-off). We hypothesize a diachronous collision in the UDMA, first in the southeastern segments, and subsequently in the central UDMA. These findings bear important implications for the geodynamic evolution of the Zagros orogen and run counter to a model suggesting that the collision initiated in the northwest to central and propagated progressively to the southeast along the Zagros suture zone.

1. Introduction

Subduction zones are significant regions for exchanging mass and energy between the mantle and crust, as well as the key location where continental crust forms, grows, and modifies (*e.g.,* De Celles et al., 2009; Ducea and Barton, 2007). Active continental margins are collages of the products of long-lived magmatic activities (*e.g.,* ≥100 My) which represent convective influx of asthenospheric mantle to shallower depths following lithospheric extension, separated by magmatic pauses, *e.g.,* influxes and lulls (*e.g.,* Paterson and Ducea, 2015). High-flux magmatic events, *i.e.,* flare-ups, are accompanied by geochemical and isotopic modifications in the upper mantle (including sub-continental lithospheric mantle; SCLM) and lowermost crust which can be diagnosed *via* investigation of mafic lavas (*e.g.,* De Celles et al., 2009; Ducea and Barton, 2007). The lithospheric mantle yields juvenile mafic magmas with unradiogenic $^{87}Sr/^{86}Sr$ ratios and correspondingly

* Corresponding authors.
E-mail addresses: shahrouz.babazadeh@gmail.com (S. Babazadeh), masdanto@unina.it (M. D'Antonio).

https://doi.org/10.1016/j.chemgeo.2024.122247
Received 24 February 2024; Received in revised form 18 June 2024; Accepted 20 June 2024
Available online 21 June 2024

radiogenic Nd isotopes; however, flare-ups are dominated by felsic magmas which show "crustal" signatures, *i.e.,* highly radiogenic Sr isotopes (*e.g.,* Burns et al., 2015). Flare-ups are characterized by initial emplacement of voluminous high-magnesian lavas (*e.g.,* basalts and andesites with hydrous tholeiitic to calc-alkaline affinity; Grove and Kinzler, 1986; Stern, 2002), and they conclude with differentiated (*i.e.,* silicic) lavas that record cannibalization of continental crust. Exhumed plutonic units reveal that flare-ups modify significant amounts of continental crustal and lithospheric materials and result in higher $^{87}Sr/^{86}Sr_{(t)}$ and lower εNd–εHf values in the magmatic products (*e.g.,* Ducea et al., 2015; Moghadam et al., 2023). However, flare-up magmatism without these characteristic isotopic signatures has recently been reported in some continental arcs (*e.g.,* Fiordland, New Zealand, and South American Cordillera; Decker et al., 2017; Ardill et al., 2018; Martínez Ardila et al., 2019; Attia et al., 2020).

The Cenozoic magmatism of Iran records an archetypal Andean-type magmatic belt that sheds light on deciphering the temporal evolution of convergent plate margins. Across the Zagros Orogeny, including the Urumieh–Dokhtar magmatic arc (UDMA; Fig. 1a), numerous mafic units occur of dominantly calc-alkaline, and rarely potassic, affinity that reflect complex temporal–spatial evolution of subduction in a paleo-arc zone. The central segment of the UDMA (*i.e.,* 32° 30′ N to 36° 00′ N; ~500 km of ~2000 km total UDMA length; Fig. 2) is an epitome of volcanic–plutonic sequences reflecting the Cenozoic flare-ups history of the Zagros Orogeny. Three distinct magmatic episodes spanning *pre-* to *post*-collisional events have been recorded from this magmatic segment: a major episode at 56–36 Ma, subordinate at 26–15 Ma, and rare at <10 Ma (*e.g.,* Babazadeh et al., 2024b). Such magmatic episodes have not been fully documented previously in other segments of the UDMA, nor in NE Iran along the UDMA rear-arc. The present study concerns *pre*-collisional mafic to felsic plutonic rocks within the central segment of the UDMA, from Kajan (Fig. 1b) where the mafic samples record magmatism outside the aforementioned magmatic episodes. Previously, Golkaram et al. (2016) used field observation and geochemical data to infer a Late Miocene–Pliocene age along with *syn-* to *post*-collisional tectonic setting for the magmatism of the southwestern Kajan region. From a geodynamics point of view, the prolonged "flare-up" magmatism in the UDMA is associated with Armenia where coeval calc-alkaline to high-K calc-alkaline magmatism are widely reported (*e.g.,* Chiu et al., 2013; Rezeau et al., 2018; Grosjean et al., 2022). The systematic cessation of magmatism following the collision between Arabia and Eurasia progressively from northwest (in Meghri) to southeast (in SE

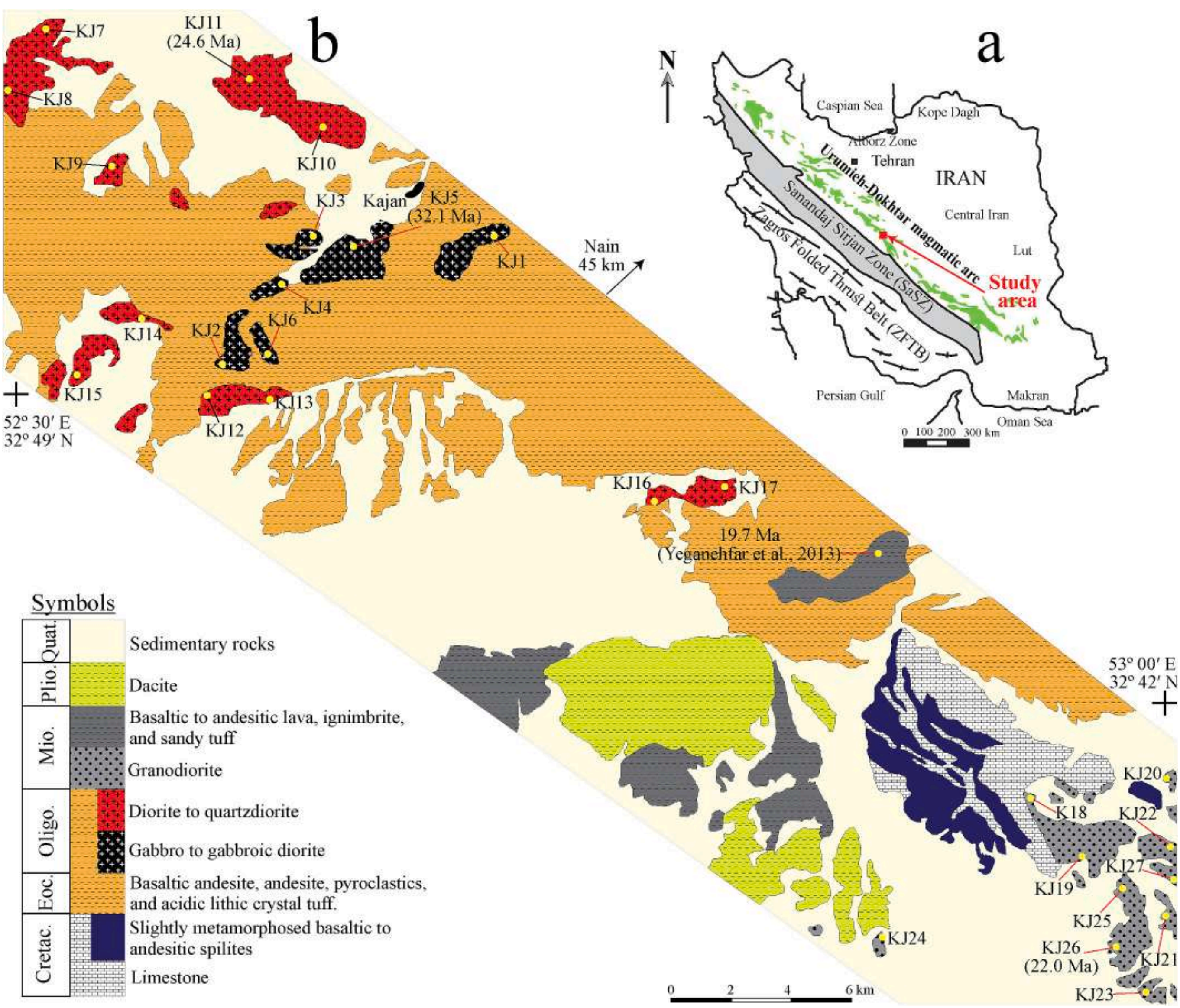

Fig. 1. (a) Simplified overview map of Iran showing the major structural units, and (b) geological map of the study area with approximate sample locations.

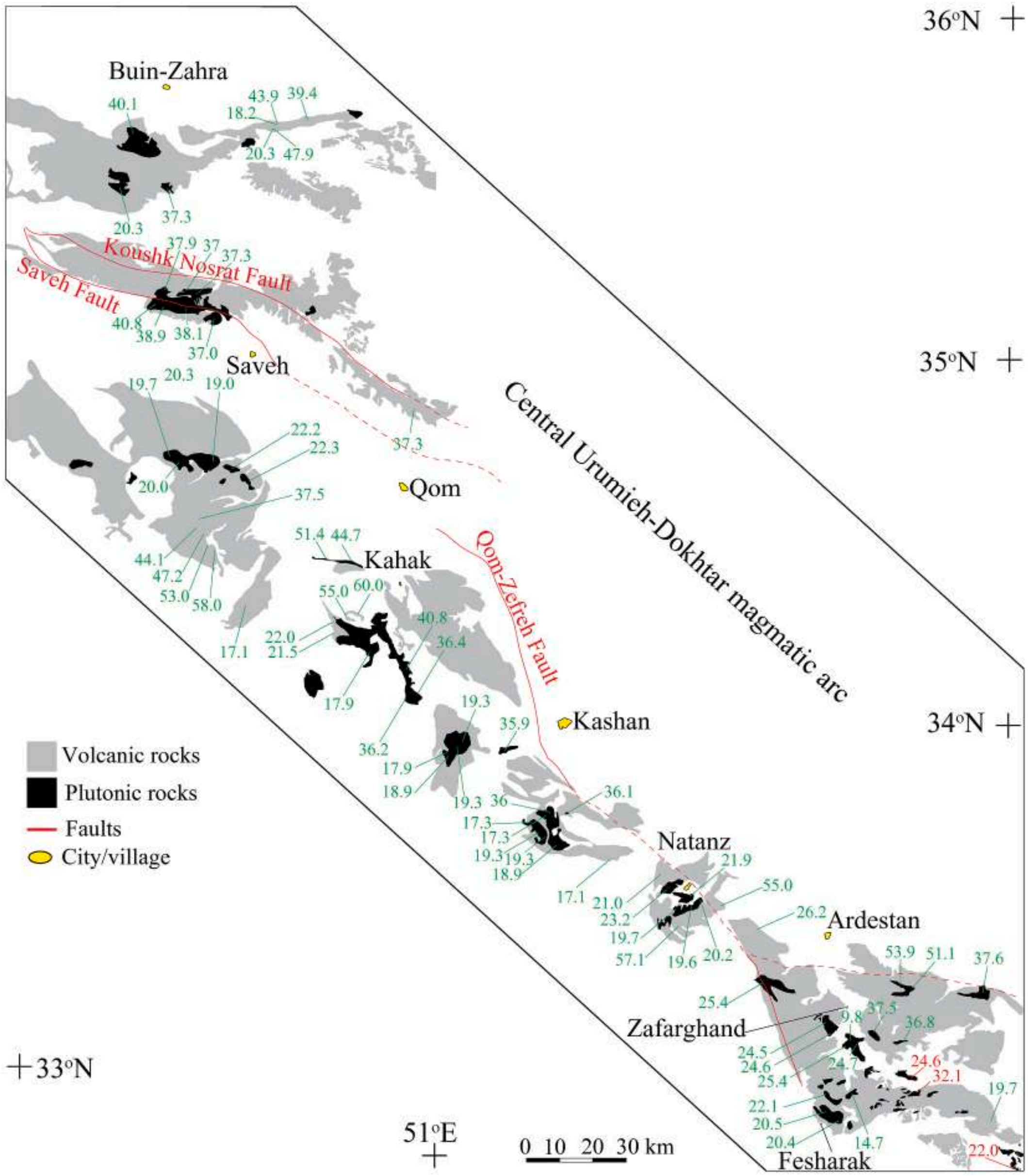

Fig. 2. Distribution of Cenozoic magmatic rocks in the central UDMA with compilation of published age data.

UDMA) is suggested and attributed to the notion of oblique and diachronous collision between the continental plates (*e.g.,* Chiu et al., 2013). Considerable debate persists regarding the Turkish branch of the Neo-Tethyan Ocean and timing of initial Arabian collision in the Eastern Anatolia Magmatic Belt (EAMB), *e.g.,* Eocene (*e.g.,* İmer et al., 2015; Schleiffarth et al., 2018), Oligocene (*e.g.,* Agard et al., 2005; Allen and Armstrong, 2008; Karaoğlan et al., 2016; McQuarrie and van Hinsbergen, 2013), Middle Miocene (*e.g.,* Faccenna et al., 2006; Schildgen et al., 2014; Ekici, 2016), and Middle-to Late Miocene (*e.g.,* Keskin et al., 1998; Keskin, 2003, 2007; Şengör et al., 2008; Okay et al., 2010; Karaoğlan et al., 2016; Ekici, 2016). Nevertheless, a progressive initiation of steepening and rupturing of the subducted slab has also been suggested since the systematic westward extension of the EAMB reached central Anatolia following the progression of collision and arc maturity (*e.g.,* Rabayrol et al., 2019). In both the Armenia and Turkey branches, the propagation of the tearing (*i.e.,* break-off) occurred after slab steepening and rollback throughout the magmatic belts.

We present new bulk rock major–trace element data, zircon U–Pb–Hf isotopic values, Sr–Nd–Pb isotopic analyses, and crystal size distribution (CSD) data for the Kajan region to further decipher the genetic roles of mantle and crust, and the geodynamic evolution of the central segment of UDMA in the course of the Oligocene–Miocene high-flux magmatic episodes. Our focus on data from central- to SE UDMA allows us to propose an interpretation that runs counter to the previous hypotheses suggested for Iran, *i.e.,* it does not support Neogene emplacement related to the collision events, nor cessation of slab rollback and initiation of break-off, nor a progressively diachronous collision toward SE UDMA, but provides a broader temporal perspective for the magmatism of central UDMA.

2. Geological setting

2.1. Geological setting of the Urumieh–Dokhtar magmatic arc

Cenozoic magmatism in Iran records the final stage of subduction of the Neo-Tethyan Ocean in the Zagros Orogeny. Subduction initiated at ~95 Ma (*e.g.,* Late Cretaceous; Stern et al., 2021) and lasted until the Quaternary (*e.g.,* Verdel et al., 2011; Pang et al., 2013; Chiu et al., 2013 and references therein; Fedele et al., 2023; Babazadeh et al., 2023, 2024a, 2024b; Moghadam et al., 2022a, 2022b, 2023; Honarmand et al., 2014, 2024). Despite general consensus on gradual change in tectonic regime from Late Cretaceous extension to contraction during the Early- to Middle Paleocene, considerable debate persists regarding the timing of collision between the Iranian and Arabian plates, interpreted as either Early Oligocene (~32–27 Ma; Agard et al., 2011; McQuarrie and van Hinsbergen, 2013; Moghadam et al., 2022a, 2022b) or Middle Miocene (~15–10 Ma; Chiu et al., 2013; Pang et al., 2013; Yeganehfar et al., 2013; Babazadeh et al., 2017, 2023; Raeisi et al., 2020, 2021). The scenario is even more complicated as different geodynamic mechanisms have been put forward for the collision, *e.g.,* from a "*soft*" collision at ~32 Ma (Early Oligocene) (*e.g.,* Allen and Armstrong, 2008; Mouthereau et al., 2012; Tadayon et al., 2017), to a "*hard*" collision at ~20 Ma (*e.g.,* Madanipour et al., 2013, 2017; Moghadam et al., 2022a, 2022b). The former mechanism was accompanied by lower rate of deformation, uplift, and exhumation. The latter is thought to be the main reason for shortening and thickening of Iranian continental crust. Moghadam et al. (2022a) divided the whole history of magmatic pulses occurring during the Zagros Orogeny into two temporally distinct phases, first at ~80–70 Ma, and second at ~50–0 Ma, and visualized a "slab break-off" geodynamic model for the southeast to central UDMA from the Oligocene onward; this model is not completely in line with the "slab rollback" mechanism proposed by many scholars for the central UDMA at Oligocene to Early Miocene time (*e.g.,* Verdel et al., 2011; Chiu et al., 2013; Sarjoughian et al., 2018, 2020; Kazemi et al., 2019; Nouri et al., 2018, 2021; Sepidbar et al., 2019; Babazadeh et al., 2017, 2019b, 2023, 2024a, 2024b; Raeisi et al., 2020, 2021, 2024). Conversely, Babazadeh et al. (2023) illustrated that the ~25–18 Ma magmatic rocks of the central UDMA are dominantly positioned to the west (*e.g.,* toward Sanandaj-Sirjan Zone) whereas those dating from ~42–38 Ma are in the east (*e.g.,* toward Central Iran). Babazadeh et al. (2023) interpreted that, in response to the slab rollback (*e.g.,* slab retreat from northeast to southwest), the magmatic front of the central UDMA apparently migrated ~40 km from the northeastern to southwestern segments between ~42 and ~ 18 Ma (see Fig. 11 of Babazadeh et al., 2023). Analysis of geochronologic, geochemical, and isotopic data by Babazadeh et al. (2021a) led to the terms "*High Alumina*" for *pre*-collisional (*i.e.*, ~47–17 Ma) and "*Low Alumina*" for *post*-collisional magmatism of the UDMA. According to ~20 Ma as the starting time of main collision (as per Moghadam et al., 2022a), the youngest magmatic phase of the rocks of this study could not be emplaced within the collision context.

2.2. Geological outline of the study area and sample selection

The plutonic rocks studied here are located ~75–90 km southeast of Ardestan, and ~ 30–45 km west to southwest of Nain (Fig. 1b). The oldest exposed stratigraphic unit is Cretaceous limestone which is intruded by slightly metamorphosed basaltic to andesitic spilites. Previous studies reveal the presence of Late Eocene (U—Pb age ~ 37 Ma) and Miocene (K—Ar age ~ 19 Ma) volcanic suites (*e.g.,* basaltic andesite, andesite, pyroclastics, and acidic lithic crystal tuff; Yeganehfar et al., 2013) as the dominant rock types which are exposed in a broadly NW–SE trending belt over an area of ~65 km^2. Exposure of volcanic--plutonic rocks is elongated parallel to the strike of the large-scale NW–SE Qom–Zefreh Fault which stretches along the central UDMA (Fig. 2). Widespread centimeters to meter thick dikes, *e.g.,* basaltic andesite and aplite, with NNW–SSE orientations (*i.e.,* following the Qom–Zefreh Fault) crosscut the host rocks. The different Kajan plutonic rocks show spatially systematic exposures without reciprocal contacts in the field. Dioritic rocks are exposed in the northern segment of the mapped area; toward the center gabbroic outcrops occur, and in the southern part of the mapped area a suite of granodiorites is exposed. The plutons are, marginally, surrounded by volcanic rocks.

From the study area, we collected twenty-seven representative plutonic samples (including 6 gabbros, 11 diorites, and 10 granodiorites) for bulk-rock major and trace element analyses. We determined zircon U–Pb–Hf geochronology data from three samples, radiogenic Sr–Nd–Pb isotopic data from 14 samples (including 5 gabbros, 4 diorites, and 5 granodiorites), and crystal size distribution (CSD) data from 1050 plagioclase grains. The gabbroic to granodioritic rocks are composed of variable amounts of euhedral to subhedral- and well-developed twin lamellae plagioclase; in some cases, plagioclase is partly replaced by secondary minerals (*e.g.,* sericite), especially in gabbros (Figs. 3a–d). Clinopyroxene is the most abundant ferromagnesian mineral in the gabbroic rocks whereas amphibole (and to lesser extent biotite) is the ferromagnesian mineral in the diorite and granodiorite. In detail, gabbroic rocks are composed of plagioclase (~80–85 vol%; 1–4 mm length) and clinopyroxene (~15–20 vol%; up to 2 mm length), which are commonly intergranular in texture. The diorites to quartz diorites are composed of plagioclase (~65–75 vol%) and subhedral hornblende (~10–15 vol%; up to 2 mm length) with variable amounts of biotite (up to 5 vol%) and allotriomorphic quartz (up to 5 vol%). Granodiorites exhibit a granular to microgranular porphyritic texture and comprise plagioclase (~50 vol%), quartz (~30 vol%), alkali feldspar (~15 vol%), and minor hornblende (~5 vol%). The ferromagnesian minerals are occasionally altered to chlorite. The investigated samples contain Fe—Ti oxides and zircon as principal accessory minerals.

3. Analytical methods and procedures

We applied multiple analytical techniques to study the Kajan magmatic rocks: (1) Inductively Coupled Plasma Atomic Emission Spectrometry (ICP–AES), and Inductively Coupled Plasma Mass Spectrometry (ICP–MS) to determine whole rock contents of major, trace and rare earth elements (REE) (ACME Analytical Laboratories Ltd., Canada); (2) Cathodoluminescence (CL) imaging of zircons and (3) Laser Ablation Multi Collector Inductively Coupled Plasma Mass Spectrometry (LA–MC–ICP–MS) to determine zircon U—Pb ages (Institute of Mineral Resources, Chinese Academy of Geological Sciences, Beijing, China); (4) Neptune Plus MC–ICP–MS (Thermo Fisher Scientific, Germany), in combination with the GeoLas 2005 (Wuhan Sample Solution Analytical Technology Co., Ltd., China); and (5) Triton Plus Thermal Ionization Mass Spectrometry (TIMS) to determine whole rock Sr—Nd isotopic ratios (Dipartimento di Scienze della Terra, dell'Ambiente e delle Risorse, University of Napoli Federico II, Naples, Italy), and Pb isotopic ratios (Analysis and Testing Research Center of the Beijing Research Institute of Uranium Geology, Beijing, China). Details on the analytical methods and procedures are given in Appendix 1, along with information on quality that was assured.

4. Results

4.1. Whole-rock geochemistry

Supplementary Table 1 lists whole-rock major, trace and rare earth element analyses of the collected plutonic rocks from the Kajan region. The data show a wide compositional spectrum, *e.g.,* SiO_2 49.53–69.05 wt %, Al_2O_3 15.42–19.48% wt%, TiO_2 0.45–1.08 wt%, MgO 0.99–7.68 wt %, and plot in the gabbro, diorite and granodiorite fields on $Na_2O + K_2O$ *vs.* SiO_2 diagram (Middlemost, 1994; Fig. 4a). The mafic rocks conform to the high-Al melts definition (*i.e.,* $\geq$ 18 wt%; as per Schiano et al., 2004), and follow a calc-alkaline trend on the K_2O *vs.* SiO_2 plot (Fig. 4b). The loss on ignition (LOI) values of the rocks are up to 2.6 wt%. No compositional gaps are evident in Harker plots, and several of them establish strikingly linear trends (Fig. 4c–h).

Fig. 5 illustrates representative trace and rare earth element (REE) patterns with their abundances normalized to primitive mantle and chondrite, respectively. The data have rather parallel patterns with the lowest trace element abundances in gabbroic rocks, and gradually higher abundances in dioritic and granodioritic samples. On primitive mantle-normalized trace element patterns, data follow homogeneous

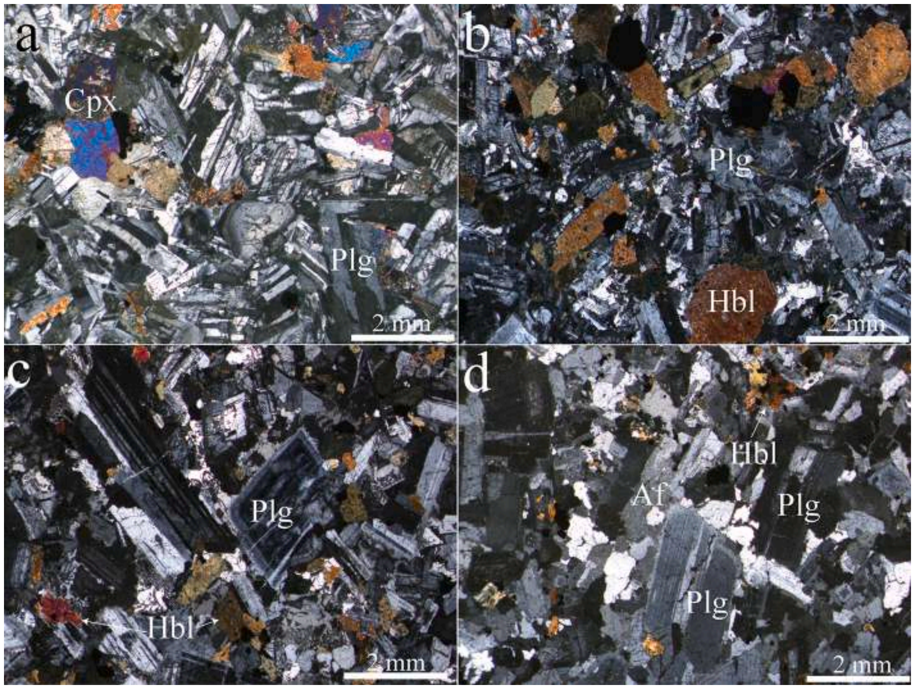

Fig. 3. (a) Representative photos showing plagioclase and pyroxenes in Kajan gabbro (sample KJ5). (b and c) Plagioclase and amphibole in diorites (samples KJ8 and KJ11, respectively), and (d) Plagioclase and alkali feldspar in granodioritic sample KJ26. Symbols: Plg = plagioclase; Af = alkali feldspar; Cpx = clinopyroxene; Hbl = hornblende.

geochemical trends, *e.g.,* enrichment in large ion lithophile elements (LILE: Rb, Th, U, K), and depletion or moderate enrichment in high-field strength elements (HFSE: Nb, Ta, Zr), alongside a remarkable positive Pb anomaly. Negative anomalies are present for some HFSE, although not remarkably and consistently all over the suite. REE patterns show variable light REE (LREE) enrichment, *e.g.,* up to 20 times in mafic, and up to 50 times in felsic samples, with $(La/Lu)_{cn}$ = 1.93–5.21, and flat middle and heavy REE (MREE and HREE) patterns with $(La/Yb)_{cn}$ = 1.94–6.05, $(La/Sm)_{cn}$ = 1.46–4.63, and $(Gd/Yb)_{cn}$ = 1.04–1.33 (Figs. 5b, d and f). Negative Eu anomalies gradually deepen from the mafic to felsic samples. The chondrite-normalized REE profiles display the lack of marked REE-pattern tetrad effects (TE_{1-3} = 0.97–1.01; Supplementary Table 1), ruling out melt–hydrothermal fluid interactions (typically F– and Cl–rich) (*e.g.,* Babazadeh et al., 2014, 2021b; Rostami et al., 2014; Raeisi et al., 2019). The remarkably fractionated REE patterns, high LILE/HFSE, high LREE/HREE, and negative Nb–Ta–Ti anomalies are in line with the universally recognized geochemical signatures of continental margin arc-like igneous rocks (Figs. 5a, c and e).

4.2. U—Pb geochronology and Lu—Hf isotopes

Three samples of the representative mafic to felsic plutonic rocks were dated by the U—Pb zircon method (*i.e.,* KJ5, KJ11, and KJ26; Supplementary Table 2). Zircons in the mafic samples are relatively scarce, and without concentric zonation. As illustrated by CL images, analyzed zircon grains in the evolved samples are prismatic and large (~180 μm) to medium and stubby (<100 μm), with dark unzoned cores and well-developed concentric zonation in mantle and rims, the typical textures of zircons that show they are of magmatic origin (Fig. 6). Nine zircon analyses from gabbroic sample KJ5 (SiO_2 = 53.20 wt%) yield a concordia age of 32.1 ± 0.3 Ma (MSWD = 0.2) and weighted mean $^{206}Pb/^{238}U$ age of 31.9 ± 0.3 Ma (MSWD = 0.2) (Fig. 6a). The dioritic sample KJ11 (SiO_2 = 60.08 wt%) gives a concordia age of 24.6 ± 0.2 Ma (MSWD = 2.3) and weighted mean $^{206}Pb/^{238}U$ age of 24.5 ± 0.1 Ma (MSWD = 1.3, n = 18) (Fig. 6b). The granodioritic sample KJ26 (SiO_2 = 68.09 wt%) gives a concordia age of 22.0 ± 0.2 Ma (MSWD = 1.2) and weighted mean $^{206}Pb/^{238}U$ age of 21.9 ± 0.1 Ma (MSWD = 1.4, n = 22) (Fig. 6c). Although zircon saturation occurs in evolved magmas, it is not unusual finding magmatic zircon in mafic rocks, which has been previously recorded both elsewhere in the UDMA and worldwide (*e.g.,* Kaczmarek et al., 2008; Chiu et al., 2013; Wang et al., 2015; Ejima et al., 2018; Shang and Chen, 2020; Azizi et al., 2020; He et al., 2020; Babazadeh et al., 2021a, 2023, 2024a, 2024b; Shao et al., 2021; Moghadam et al., 2022b; Moradi and Ghorbani, 2022; Kara et al., 2022; Wu and Qin, 2022; Nicollet et al., 2022; Du et al., 2023).

Supplementary Table 3 presents the measured $^{176}Lu/^{177}Hf$ and $^{176}Hf/^{177}Hf$ ratios of zircons from Kajan plutonic rocks. The $^{176}Hf/^{177}Hf$ values for study zircons range from 0.28132 to 0.28255 corresponding to $\varepsilon Hf_{(t)}$ of −0.7 to +5.9 (Fig. 7a). Considering $^{176}Lu/^{177}Hf$ = 0.015 as an average of the continental crust (as per Griffin et al., 2002), the $^{176}Hf/^{177}Hf$ value of zircons yield T_{DM} modal ages of 492 to 728 Ma, and T^{C}_{DM} modal ages of 596 to 926 Ma.

4.3. Sr–Nd–Pb isotopes

Supplementary Table 4 lists Sr—Nd isotopic values of fourteen representative samples from the Kajan region. The initial (age-corrected) $^{87}Sr/^{86}Sr$ values are 0.7047 to 0.7059, and $^{143}Nd/^{144}Nd$ are 0.51267 to 0.51273, corresponding to positive $\varepsilon Nd_{(t)}$ ranging from 1.18 to 2.25. On the plot of $^{87}Sr/^{86}Sr_{(t)}$ *vs.* $\varepsilon Nd_{(t)}$ (Fig. 7b), the data points plot within the OIB field, and concentrate close to the bulk silicate earth (BSE) but rightward deviated toward an enriched mantle component (EMII-type), and sediment fluids and/or alteration. The isotopic values of the Kajan rocks are analogous to those reported from the Eocene to Middle Miocene UDMA magmatic rocks (*e.g.,* Dargahi et al., 2010; Yeganehfar et al., 2013; Honarmand et al., 2014; Golkaram et al., 2016; Babazadeh et al., 2017; Babazadeh et al., 2021a, 2023, 2024a, 2024b; Sarjoughian et al., 2018, 2019, 2020, 2022; Chekani Moghadam et al., 2018; Haghighi Bardineh et al., 2018; Nouri et al., 2018, 2021; Kazemi et al., 2019, 2020, 2024; Sepidbar et al., 2019; Nazarinia et al., 2020; Moradi et al., 2021; Moradi and Ghorbani, 2022; Moghadam et al., 2022a, 2022b) and Eocene NE Iran (*i.e.,* UDMA rear arc; Mazhari et al.,

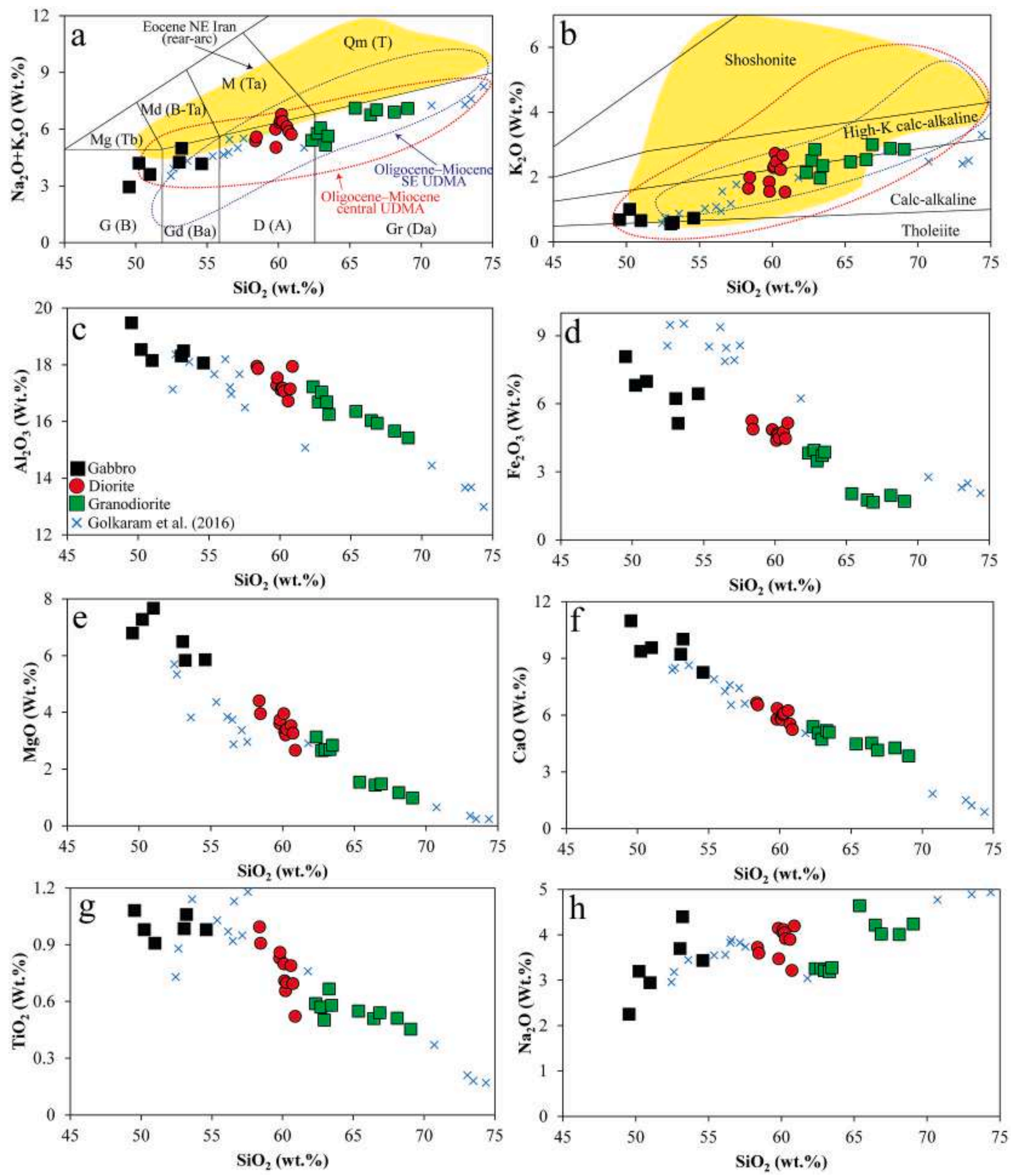

Fig. 4. Geochemical diagrams. (a) Total alkalis *versus* silica (Middlemost, 1994). The plutonic samples plot in the gabbro, diorite and granodiorite fields. (b) SiO_2 *vs.* K_2O (Peccerillo and Taylor, 1976). (c–h) Major element Harker variation diagrams for mafic to felsic plutonic rocks from the Kajan area.

2017; Sepidbar et al., 2019; Moghadam et al., 2015, 2020, 2023; Alizadeh et al., 2023; Azizi et al., 2020). For the study rocks, the average $T_{DM(Nd)}$ model ages cluster around 474 to 568 Ma (Supplementary Table 4), concurrent with Cadomian orogeny events in Iran (*e.g.,* Honarmand et al., 2014; Moghadam et al., 2015; Moghadam et al., 2020, 2023; Nayebi et al., 2023, 2024; Alizadeh et al., 2023).

The Kajan samples have a relatively restricted range in initial Pb isotopic compositions: $^{206}Pb/^{204}Pb_{(t)} = 18.21$ to 18.36, $^{207}Pb/^{204}Pb_{(t)} =$ 15.48 to 15.55, and $^{208}Pb/^{204}Pb_{(t)} = 37.91$ to 38.22 (Supplementary Table 5) resembling magmatic rocks reported from OIB, Indian Ocean MORB, Zagros ophiolite, and *pre*-collisional Ardestan magmatic rocks, and do not fit well with Eocene NE Iran (*i.e.,* UDMA rear arc), Niyasar (west of Kashan; Fig. 2) and Kahak (south of Qom; Fig. 2) magmatic rocks. As per uranogenic-Pb diagram (Figs. 7c and d), the data plot within the OIB field, namely, between depleted MORB mantle (DMM) and subducting sediments (SED) (*e.g.,* Stracke et al., 2005; Kimura et al., 2014; Moghadam et al., 2022a, 2022b, 2023 and references therein).

5. Discussion

5.1. Evaluation of geochemical data

The trends of major oxides on binary Harker plots (Figs. 4c–h; see also Appendix Fig. 1) argue for an early crystallization of high-Ca pyroxene, calcic plagioclase, and amphibole. However, similar trends might have been caused by mixing between mafic and felsic magmas. On the primitive mantle-normalized profiles, depletions of Ba, Sr, P, and Ti suggest fractional crystallization of Sr- and Ba-rich minerals (*e.g.,* plagioclase), P-rich minerals (*e.g.,* apatite), and clinopyroxenes and Ti-rich minerals (*e.g.,* titanomagnetite). On chondrite-normalized REE profiles, the samples display moderately fractionated patterns from LREE to MREE (Figs. 5a, c and e), and rather flat patterns for M–HREE sections. The latter features argue against the presence of considerable garnet, either in the mantle residue or as part of the fractionating assemblage in the magma. The low abundances of HREE, Ti, Sm, and Zr

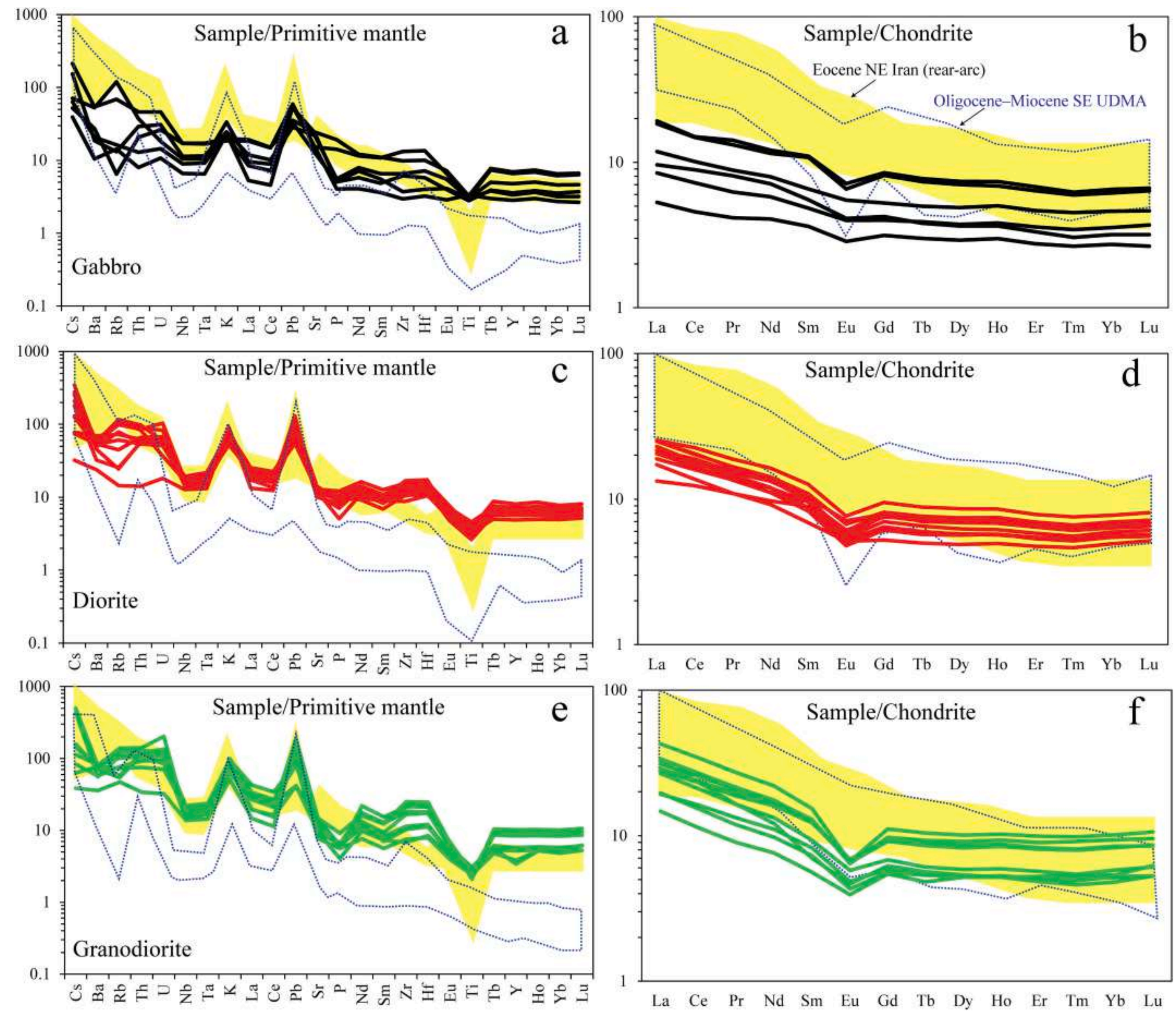

Fig. 5. Primitive mantle normalized trace element and chondrite-normalized REE patterns for the Kajan plutonic rocks. Normalization values are from Sun and McDonough (1989).

together with slightly concave–upward pattern in MREE section attest to amphibole and rutile stability in the magma source region. Negative anomalies for Th—U on some profiles likely reflects the presence of apatite as a fractionating phase. Rather weak negative Eu anomalies on chondrite-normalized REE profiles and a negative correlation between MgO and Al_2O_3 (not shown) in the mafic and intermediate samples place emphasis on fractionation of plagioclase rather than K-feldspar, and a high oxidation state in the magmatic system, *i.e.,* europium mostly occurring as Eu^{3+}, not Eu^{2+} (Richards et al., 2012), suggesting emplacement at shallow depth. The geochemical signatures of Kajan rocks (*e.g.,* high Al_2O_3 and moderate MgO) invoke melting of a metasomatized rather depleted mantle and crystal fractionation under low-*P* and high-f_{H2O} (*e.g.,* dissolved $H_2O \geq 6$ wt%) rather than accumulation or flotation of plagioclase (*e.g.,* Sisson and Grove, 1993). We suggest the order of crystallization is clinopyroxene (± subordinate olivine) and minor Ca-rich plagioclase segregated during the first stages of magmatic evolution, and nucleation of biotite, amphibole (±clinopyroxene) and accessory magnetite. Finally, a decrease in growth of amphibole was followed by K-feldspar and quartz fractionation in the course of the later stages of magmatic evolution. The protracted process of fractional crystallization from basic to felsic melts over geological timescales can be attributed to (*i*) large size of the magmatic chamber (*e.g.,* Marsh, 1988; Annen and Sparks, 2002; Bachmann and Bergantz, 2004, 2008), (*ii*) slow cooling rates (*e.g.,* Marsh, 1988; Putirka, 2008), (*iii*) continuous magma input (*e.g.,* Charlier et al., 2005; Marsh, 1988), (*iv*) efficient separation of crystals (*e.g.,* Cashman and Blundy, 2000; Annen and Blundy, 2008), and (*v*) complexity of magmatic processes (*e.g.,* Huber and Bachmann, 2016). Our inference of the protracted fractional crystallization through time is analogous to Eocene to Miocene magmatic suites which pertain to the long-term extent of Neo-Tethyan subduction (*e.g.,* Pang et al., 2013; Babazadeh et al., 2017, Babazadeh et al., 2023, 2024a, 2024b; Nouri et al., 2018; Omidianfar et al., 2022; Moghadam et al., 2022a,b, 2023; Fazlnia et al., 2023; Sepahi et al., 2023).

5.2. *Appraisal of mantle enrichment by subduction components*

Potassium-bearing phases, *e.g.,* amphibole and phlogopite, are the volatile-bearing minerals which mainly control LILE enrichment in the

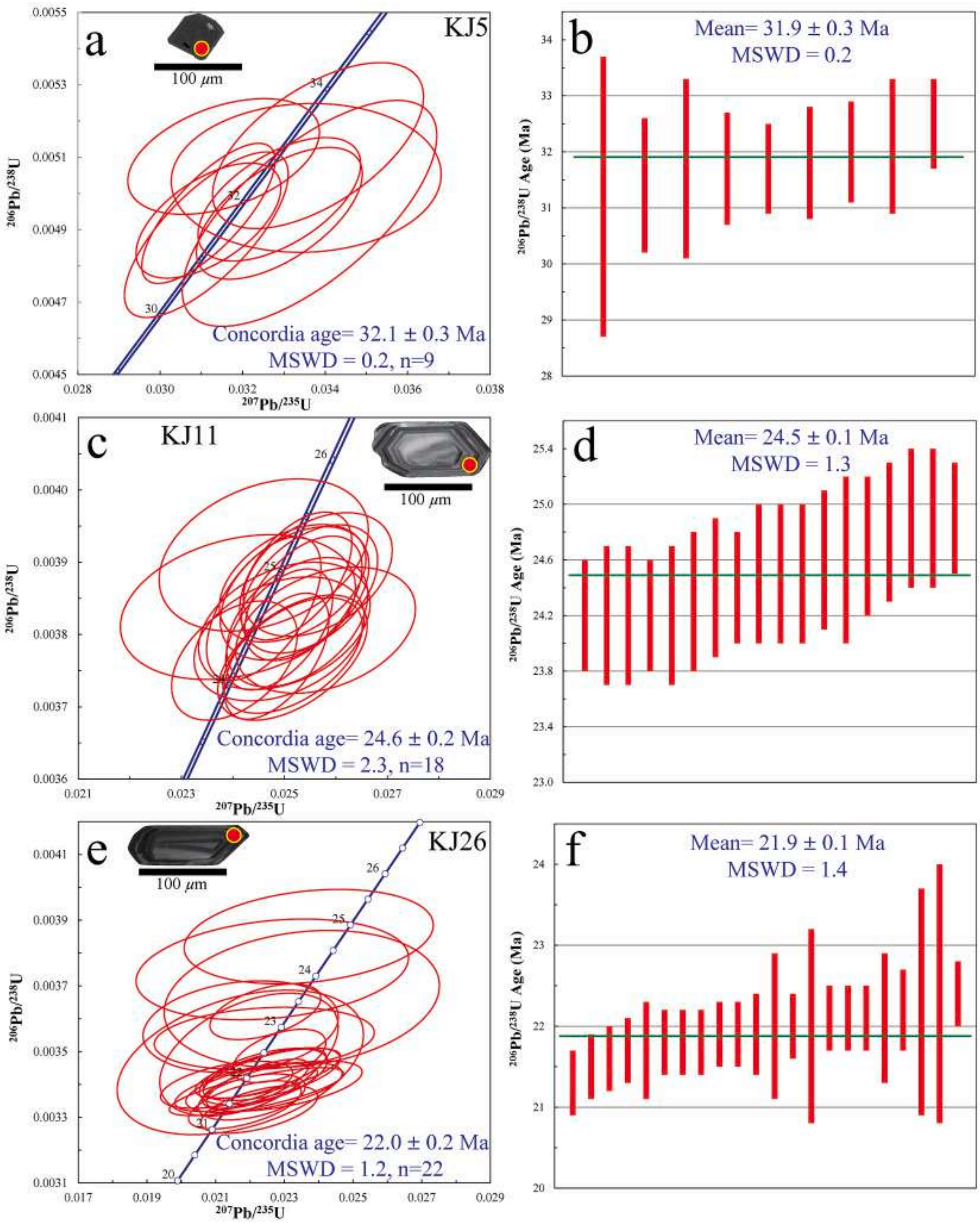

Fig. 6. Tera–Wasserburg concordia and weighted mean age diagrams showing analytical data for zircons from Kajan plutonic rocks.

mantle source of subduction-related magmas (*e.g.,* Ionov et al., 1997). Since Ba and Rb have different degrees of compatibility in phlogopite and amphibole, melts in equilibrium with phlogopite tends to have elevated Rb/Sr (>0.1) and lower Ba/Rb (<20) ratios compared to those from amphibole-bearing sources (*e.g.,* Furman and Graham, 1999). The Kajan mafic rocks (*e.g.,* Rb/Sr up to 0.15, and Ba/Rb up to 46) are in line with residues of both hydrous phases (*e.g.,* amphibole and phlogopite) during melting of a lithospheric mantle source. As amphibole is unstable in the upper mantle (*e.g.,* Juricek and Keppler, 2023), the presence of residual amphibole in the mantle source beneath Kajan suggests the lithospheric mantle is the dominant source region for mafic magmatism. Our inference is not a unique solution to elucidate the mantle signature of all Eocene to Miocene magmatic rocks; given the long-term extent of Neo-Tethyan subduction some segments of the UDMA were already characterized by sources with either residual amphibole or phlogopite (*e.g.,* Babazadeh et al., 2017, 2021a; Nouri et al., 2021).

In subduction settings, melts derived from asthenospheric mantle and traveling toward upper levels are commonly metasomatized by addition of fluids and/or melts derived from the subducting slab, including sediments. As a result, such a magma could have geochemical and isotopic signatures of arc setting (*i.e.,* enrichment of LILE relative to HFSE, and positive Pb anomalies) or oceanic islands (OIB-like) or basalt erupted at mid-ocean ridges (transitional MORB-like, *i.e.,* moderate concentrations of incompatible trace elements together with Nb–Ta–Ti anomalies in basic suites) (*e.g.,* Hofmann, 1997; Turner and Foden, 2001). The Kajan data support this inference (Figs. 5 and 7b). We thus rule out a pure asthenosphere mantle source and suggest that metasomatized mantle wedge and/or lithospheric mantle above the subducting plate were involved, as confirmed previously by the presence of both amphibole and phlogopite in the mantle source of Oligocene to

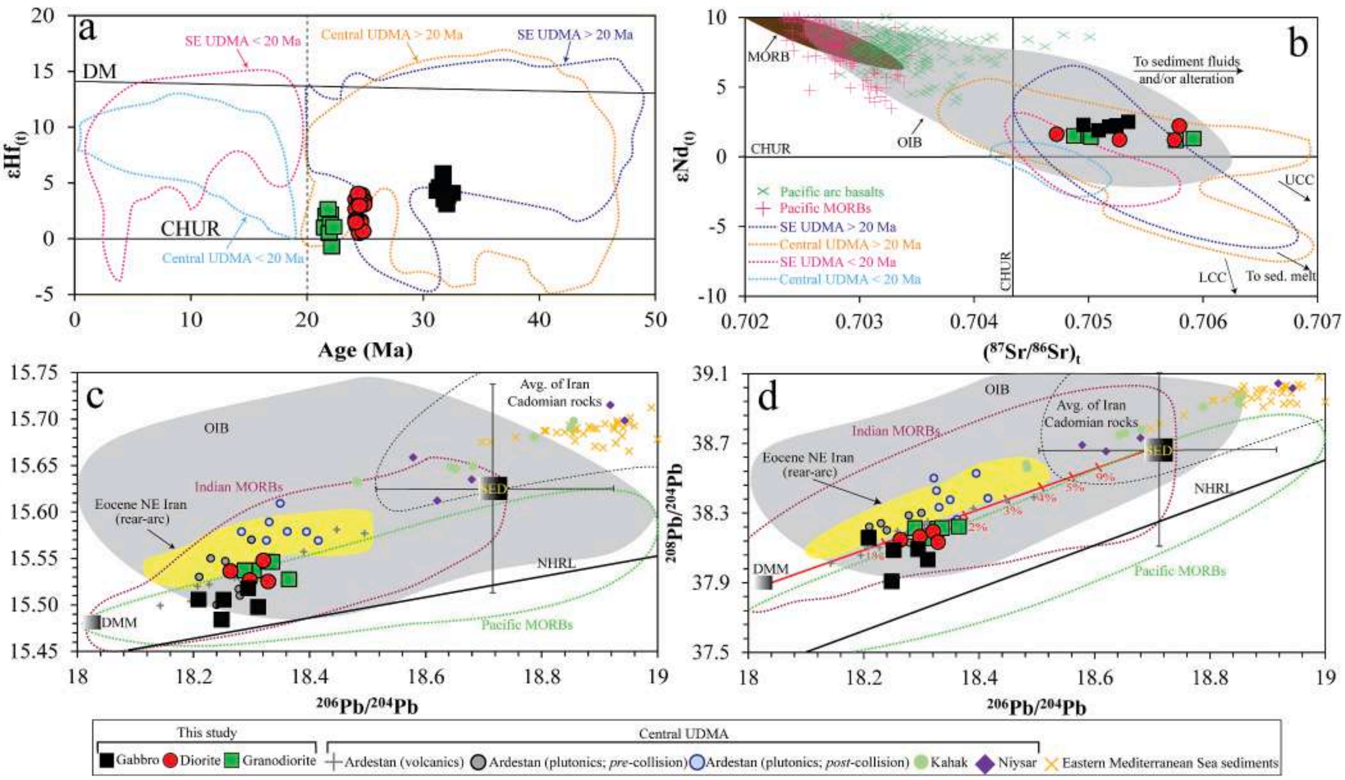

Fig. 7. (a) Plots of zircon $\varepsilon Hf_{(t)}$ *vs.* zircon U—Pb age. (b) $\varepsilon Nd_{(t)}$ *vs.* $(^{87}Sr/^{86}Sr)_t$. Data of the studies rocks plot in the mantle array field. Cadomian continental crust (CC) from Moghadam et al. (2015). (c) Plots of $^{207}Pb/^{204}Pb$ *vs.* $^{206}Pb/^{204}Pb$, and (d) $^{208}Pb/^{204}Pb$ *vs.* $^{206}Pb/^{204}Pb$. Data for Eocene NE Iran (rear-arc), central-and SE UDMA are presented in Appendix 2. Data for subducting sediments (SED) and altered oceanic crust (AOC) are from Arc Basalt Simulator version 3 (Kimura et al., 2014). Field for OIB as defined by Stracke et al. (2005).

Miocene plutonic rocks in Ardestan (*i.e.,* ~75–90 km northwest of Kajan; Babazadeh et al., 2017). Specific geochemical features, *e.g.,* moderate $^{87}Sr/^{86}Sr$ ratios (0.7047–0.7059), Sr (161–515 ppm), elevated Y (13–46 ppm) corresponding to moderate Sr/Y (3−33) ratios, are far from those typical of adakitic rocks, *e.g.,* low $^{87}Sr/^{86}Sr < 0.7045$, Y < 8 ppm, Sr > 400, and Sr/Y > 20 (as per Castillo, 2008), and thus, do not conform to melts derived from a subducting slab.

Interaction between sediments and mantle can occur either through mixing of the bulk sediment (*i.e.,* diapirs of sediment or a crust–sediment 'mélange') with peridotite, or through an influx of sediment melts and/or fluids into peridotite (*e.g.,* Elliott, 2003; Marschall and Schumacher, 2012). For the former, the sediment- or mélange diapirs would not be a 'slab component' rising off the slab, but direct subduction erosion to the mantle wedge peridotite (*e.g.,* Marschall and Schumacher, 2012; Nielsen and Marschall, 2017). As per experimental findings of Codillo et al. (2018), residual garnet is not thought to be stable in the low-pressure partial melting of the mélange diapirs. Thereby, this process would not be able to produce melts enriched in Th and without also enrichment in HREE, geochemical signatures standing in marked contrast to the Kajan samples. Turner and Langmuir (2022a, 2022b) have recently re-examined geochemistry, experimental results, physical models, and tectonic constraints to account for incompatible element differences in continental arc settings including; (*i*) the influence of thick crust, (*ii*) slab thermal structure, (*iii*) heterogeneity of the ambient mantle wedge, (*iv*) mantle wedge thermal structure, and (*v*) slab diapirs and subduction erosion. Accordingly, neither crust processes nor slab temperature models are aligned with the variety of observations. Further, the findings run counter to a significant role for transportation of bulk sediments to the wedge (*e.g.,* in a diapir or slab diapirs) and that arc compositions are most consistent with slab melting on or near the surface of the subducting plate. As per finding of Turner and Langmuir (2022a, 2022b), slab components (*e.g.,* sediment or fluid), apparently, have greater influence on depleted mantle compositions.

Among Kajan samples, varying degrees of mantle metasomatism by slab components, specifically sediments (*i.e.,* an enriched-mantle source), can be inferred from observed high Th and Pb abundances, and Th/Yb and La/Yb ratios. The Nb/Zr and Nb/Yb values and Nd—Pb isotopic variations (*i.e.,* Nb/Zr 0.05–0.14; Nb/Yb 2.7–4.7; $^{143}Nd/^{144}Nd_{(t)}$ 0.51267–0.51273; $^{206}Pb/^{204}Pb_{(t)}$ 18.21–18.36) of our samples, which resemble those of NE Iran and SE UDMA magmatic suites, but far from average of altered oceanic crust (AOC) (*i.e.,* Nb/Zr ~0.03; Nb/Yb ~1.5; $^{143}Nd/^{144}Nd_{(t)} \sim 0.51315$; $^{206}Pb/^{204}Pb_{(t)} \sim 18.53$) (Figs. 8a–d; see Appendix 2 for the references). This inference is further supported by elemental and isotopic diagrams, *e.g.,* Th/Nb *vs.* $^{206}Pb/^{204}Pb_{(t)}$ and Ba/Nb, and Ba/Th *vs.* $^{206}Pb/^{204}Pb_{(t)}$ (Figs. 9a–c). Notice that our parameters applied to the binary diagrams (*e.g.,* Figs. 8 and 9) are heuristic, selected utilizing the best constraints available for the model inputs.

To constrain the contribution of terrigenous sediments during petrogenesis, we have designated the investigated rocks for source modeling which represent the composition of the mantle melts (Figs. 9d and e). Our modeling, based upon contributions from the upper limit of OIB-like (*e.g.,* $^{143}Nd/^{144}Nd_{(t)} \sim 0.5130$; $^{206}Pb/^{204}Pb_{(t)} \sim 18.65$; Ba/La ~ 9; Ol + Opx + Cpx + Spl mineral assemblage; as per Workman and Hart, 2005) and terrigenous sediments (as per Kimura et al., 2014) reveals that the mafic samples fit well with a batch melt composed of 98.5% mantle melt and 1.5% terrigenous sediments.. That sediment contribution is lower than values calculated for NE Iran (*i.e.,* rear-arc) and SE UDMA, for which the effect of terrigenous sediments has been proposed to be up to 3% (*e.g.,* Moghadam et al., 2022a, 2022b, 2023; Babazadeh et al., 2021c, 2023; Alizadeh et al., 2023).

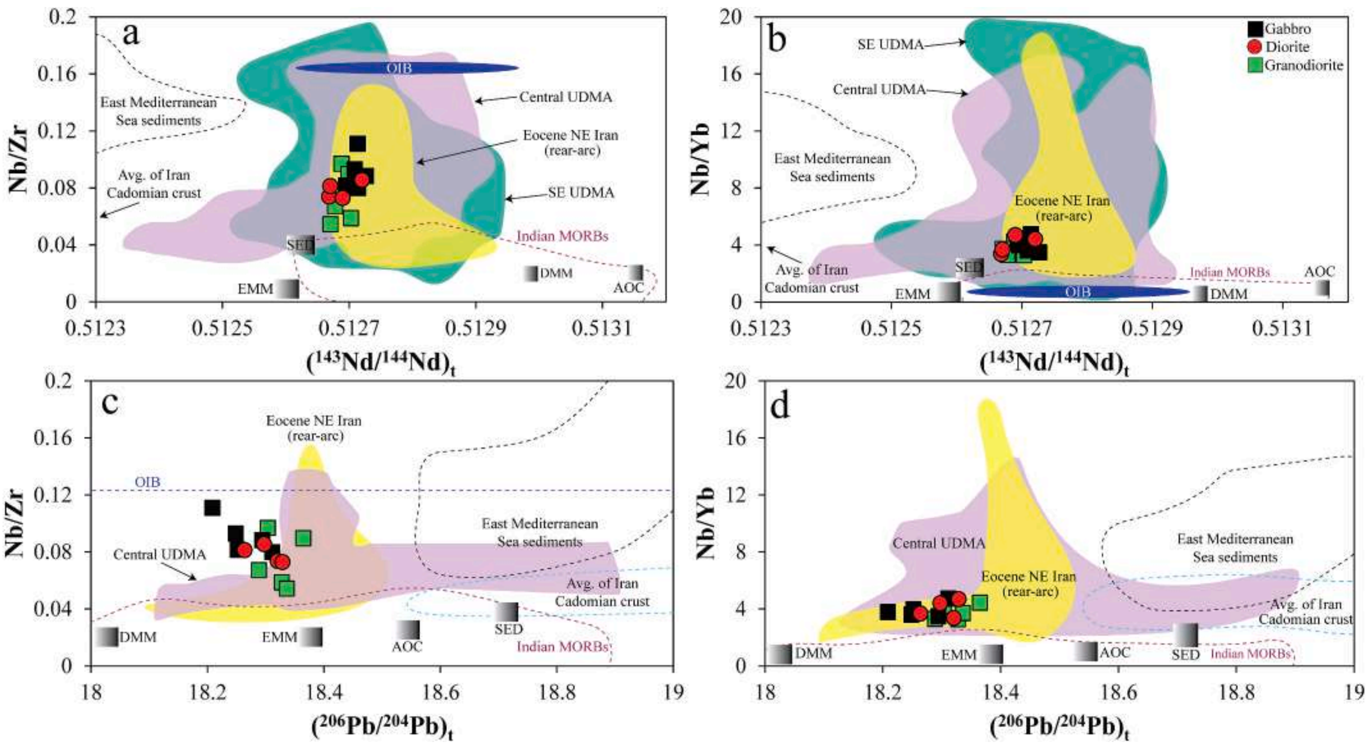

Fig. 8. (a and b) Plots of Nb/Zr and Nb/Yb *vs.* ^{143}Nd/^{144}Nd$_{(t)}$. (c and d) Plots of Nb/Zr and Nb/Yb *vs.* ^{206}Pb/^{204}Pb$_{(t)}$. Data for the composition of Eastern Mediterranean Sea sediments are from Klaver et al. (2015). DMM and EMM are depleted and enriched Indian oceanic (MORB-) mantle sources, respectively (Zindler and Hart, 1986).

5.3. Mantle signature and crustal assimilation in evolved magmas

Trace element ratios, alone or in combination with isotopic values, are widely employed as proxies to distinguish the contribution of mantle *vs.* continental crust during magma evolution. Average values of Zr/Nb and Nb/La (*i.e.,* ~11 and ~ 1, respectively) in the Kajan samples are close to those observed in the mantle (~8 and > 1, respectively) and do not argue for involvement of significant amounts of continental crust (22–25 and < 0.46, respectively; *e.g.,* Morata et al., 2005). Relative abundances of Zr—Hf and Nb—Ta (as conservative elements) can be explored to constrain whether fractionation of these element pairs was originally rooted in the mantle wedge or whether it rather mirrors assimilation-fractional crystallization (AFC) (*e.g.,* Moghadam et al., 2022a; Pearce and Peate, 1995). Mantle-derived melts retain chondritic Zr/Hf and Nb/Ta ratios, *i.e.,* Zr/Hf = 36 and Nb/Ta = 17.6–19 (Sun and McDonough, 1989). The Kajan samples have chondritic to sub-chondritic values of Zr/Hf = 30–36 and Nb/Ta = 16–17 that approach OIB- to MORB-like compositions in Nb/Ta *vs.* Zr/Hf and Th/Yb plots (Figs. 10a and b). They have Nb/Yb ratios of ~2.8 to 4.8, geochemically akin to *E*-MORB (*i.e.,* Nb/Yb ~3.5) and distinct from those of N-MORB (*i.e.,* Nb/Yb ~0.3). The average of Th/Yb, La/Yb and Nb/Ta ratios are ~0.2, ~17.12, and ~ 17.6–19, respectively, for mantle derived melts (*e.g.,* OIB- to MORB-like) and ~ 5.5, 0.3–0.6, and 11–12, respectively, for crustal derived melts (*e.g.,* Sun and McDonough, 1989; Green, 1995; Morata et al., 2005). As illustrated on Figs. 10a and b, the data establish negative correlations between Th/Yb (or La/Yb) and Nb/Ta from parental mafic (*i.e.,* Nb/Ta and Th/Yb ratios comparable to OIB- to MORB-like melts) to derivative felsic magmas (*i.e.,* Nb/Ta and Th/Yb ratios comparable to average continental crust), suggesting only small degrees of crustal assimilation.

Positive Nd isotopic values (*i.e.,* $\varepsilon Nd_{(t)}$ = 1.18–2.52) of the entire Kajan suite and Pb-isotope ratios aggregating near fields for OIB- to EMM, and Indian MORB fields (Figs. 7c and d), deviate toward the Cadomian crust of Iran (Figs. 8a–d; see Moghadam et al., 2015 for an extended discussion about the Cadomian crust), and variable but dominantly positive initial Hf (*i.e.,* −0.7 to +5.9) reinforce the evidence for a mantle source signature (*e.g.,* DePaolo and Daley, 2000). However, slightly negative initial Hf in some zircon grains (5 out of 49 spots), depletions in HFSEs (*e.g.,* Nb and Ti) relative to LILEs and LREEs, and negative Nb anomalies in some whole-rock samples attest a slight degree of heterogenity in the mantle wedge (absolute depletion) and/or metasomatization of the mantle wedge (relative depletion) *via* fluids or sediment-derived melts from the down-going oceanic slab (*e.g.,* Bindeman et al., 2005; Duggen et al., 2007; Ahmadi et al., 2019) or crustal contamination (*e.g.,* Vervoot and Kemp, 2016). On a plot of ^{143}Nd/^{144}Nd *vs.* Hf/Nd (Fig. 10c), the Kajan data form curves between mantle melt and either continental crust (CC) or global subducting sediments (GLOSS). Notice that some evidence of partial melting of the juvenile continental crust is documented in conjunction with *post*-collisional and Cu-mineralization events, *e.g.,* SE UDMA (*e.g.,* Shafiei et al., 2009; Aghazadeh et al., 2015; Lechmann et al., 2018; Raeisi et al., 2021; Moghadam et al., 2022a; Javidi Moghadam and Karimpour, 2023), Turkish Eastern Pontides (*e.g.,* Eyuboglu et al., 2012; Karsli et al., 2011, 2020; Dokuz et al., 2013, 2019), and South Armenian Block (*e.g.,* Moritz et al., 2016; Rezeau et al., 2016, 2017, 2018; Grosjean et al., 2022). Therefore, the pre-collision stage (*i.e., pre*-hard collision) of the investigated samples plausibly precludes the possibility of partial melting of juvenile continental crust, instead, speaks for more and less contribution of the old continental crust (*e.g.,* Cadomian crust) during the petrogenesis of the Kajan region– an analogous mechanism to the Eocene Kuh-e-Dom and Eshtehard, and Oligocene Ardestan, Kahak, and Kashan magmatic rocks (*e.g.,* Yeganehfar et al., 2013; Kananian et al., 2014; Babazadeh et al., 2017; Babazadeh et al., 2019a; Moradi et al., 2021; Khaksar et al., 2022). As posited by Babazadeh et al. (2017, 2019a), the Ardestan dioritic rocks, which are coeval to the investigated dioritic Kajan (*i.e.,* 24 Ma; exposed approximately 18 km to the N–NW of the investigated rocks), contain a significant number of *ca.* 550 Ma zircons (24 spots)– an evidence that further supports the contribution of the

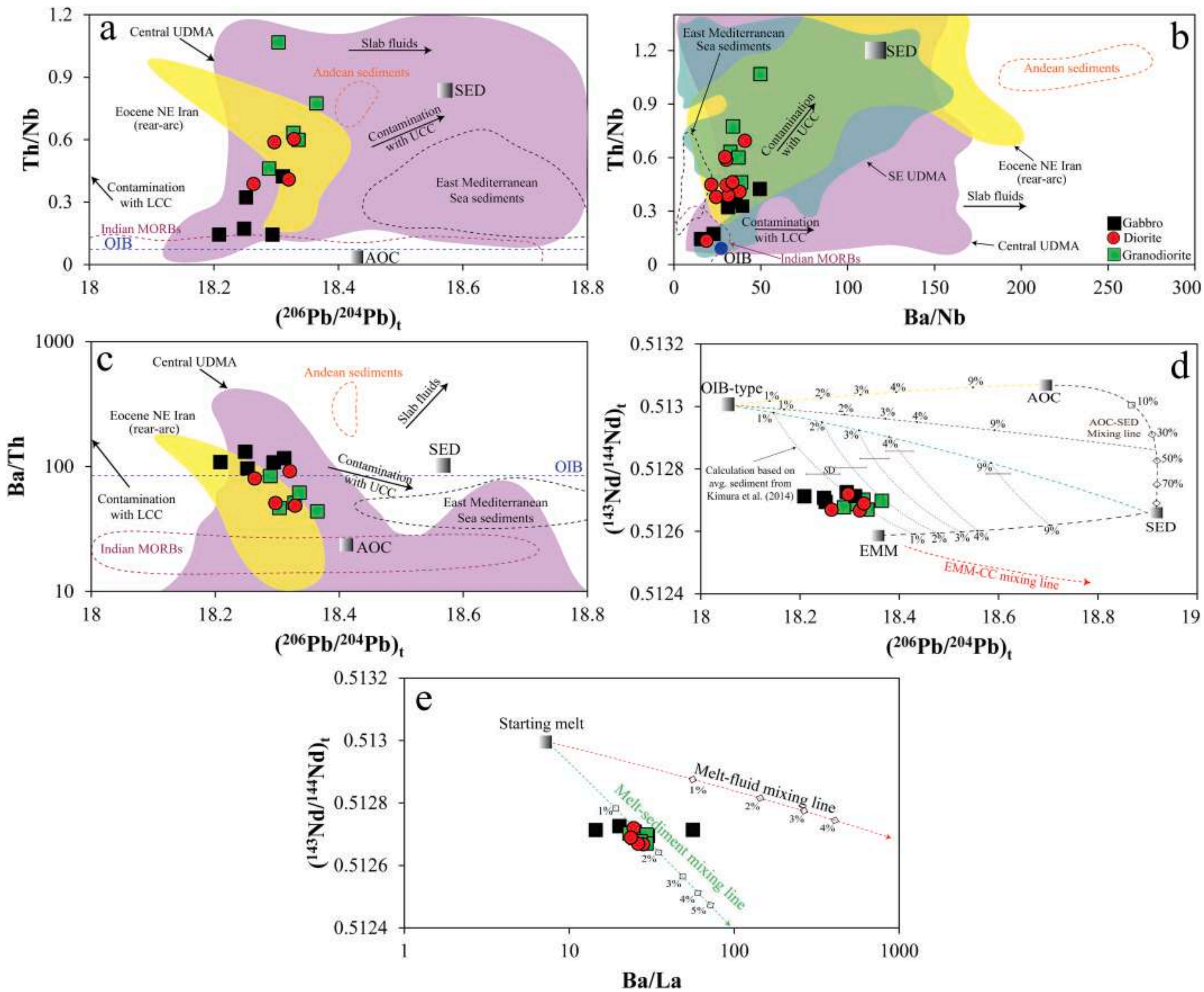

Fig. 9. (a and b) Plots of Th/Nb *vs.* $^{206}Pb/^{204}Pb_{(t)}$ and Ba/Nb. (c) Ba/Th *vs.* $^{206}Pb/^{204}Pb_{(t)}$; the data follow the sediment melt trend. (e and d) Plots of $^{143}Nd/^{144}Nd_{(t)}$ *vs.* $^{206}Pb/^{204}Pb_{(t)}$ and Ba/La; illustrating up to 1.5% enrichment by sediment-derived melts for the samples. Applying the maximum and minimum values of terrigenous sediments composition (as per Kimura et al., 2014) permits ±0.5% deviation value (*i.e.,* SD), thus from 0.5 up to 1.5% sediment contribution.

Cadomian continental crust beneath the central UDMA before the initiation of the "*hard*" collision and crustal thickening. Instead, no record of *ca.* 550 Ma zircons from the *post*-hard collision suites (*e.g.,* < 20 Ma) as well as the occurrence of Cu mineralization in association with adakitic magmatism mirror the plausible cannibalization of juvenile crust during the arc maturity.

Crystal size distribution (CSD) is a heuristic qualitative method that allows appraisal of processes occurring during transport or storage within crustal magma chambers *e.g.,* FC, AFC and/or mixing, accumulation, and cooling (see Appendix Fig. 2). The CSD method is widely used for plagioclase and pyroxene crystals (*c.f.,* Cashman and Marsh, 1988); here we employ the method for plagioclase feldspar. Straight-line CSD slopes record a batch system in steady-state conditions; by contrast, gull-wing or kinked and curved CSD profiles record inflowing and outflowing magma followed by renewal nucleation, *i.e.,* unsteady-state conditions. On binary plots of population density (ln(n), mm-4) *vs.* size (L, mm) (Supplementary Table 6; Fig. 11), the aggregate Kajan CSD profiles illustrate at most negligible displacement from the classic straight-line trend, which we interpret as supplementary evidence for a trivial role for assimilation or mixing processes. Regarding an active continental margin setting such as that of the UDMA, including Kajan, modification in melt-derived magma composition by crustal components is not far-fetched.

The crustal contribution hypothesis can be further tested by isotopic mixing mass balance modeling. Quantitative AFC mixing modeling using the parental melt– geochemically and isotopically analogous to OIB- and EMM-like (*e.g.,* $^{87}Sr/^{86}Sr_{(t)}$ ~ 0.703, $^{143}Nd/^{144}Nd_{(t)}$ ~ 0.5130; Stracke et al., 2005 and references therein) – and Cadomian upper and lower continental crust (*i.e.,* $^{87}Sr/^{86}Sr_{(t)}$ ~ 0.713 and $^{143}Nd/^{144}Nd_{(t)}$ ~ 0.5121, and $^{87}Sr/^{86}Sr_{(t)}$ ~ 0.707 and $^{143}Nd/^{144}Nd_{(t)}$ ~ 0.5112 for UCC and LCC, respectively; Moghadam et al., 2015) as endmembers best matches a mixture of 97–98% of the batch melt (*i.e.,* 98.5:1.5 of mantle melt and terrigenous sediment) and 2–3% of the UCC (Fig. 10d). This ratio corresponds to the minimum percent of assimilation of continental crust (*i.e.,* 20% to as little as 2%) by mantle-derived melts modeled for the UDMA (*cf.* Yeganehfar et al., 2013; Honarmand et al., 2014; Hosseini et al., 2017; Babazadeh et al., 2017, 2019a, 2019b, 2023, 2024a; Nazarinia et al., 2020; Asadi, 2018; Nouri et al., 2018, 2021; Sarjoughian et al., 2018, 2019, 2020, 2022; Moghadam et al., 2022a, 2022b, 2023; Sepahvand et al., 2022).

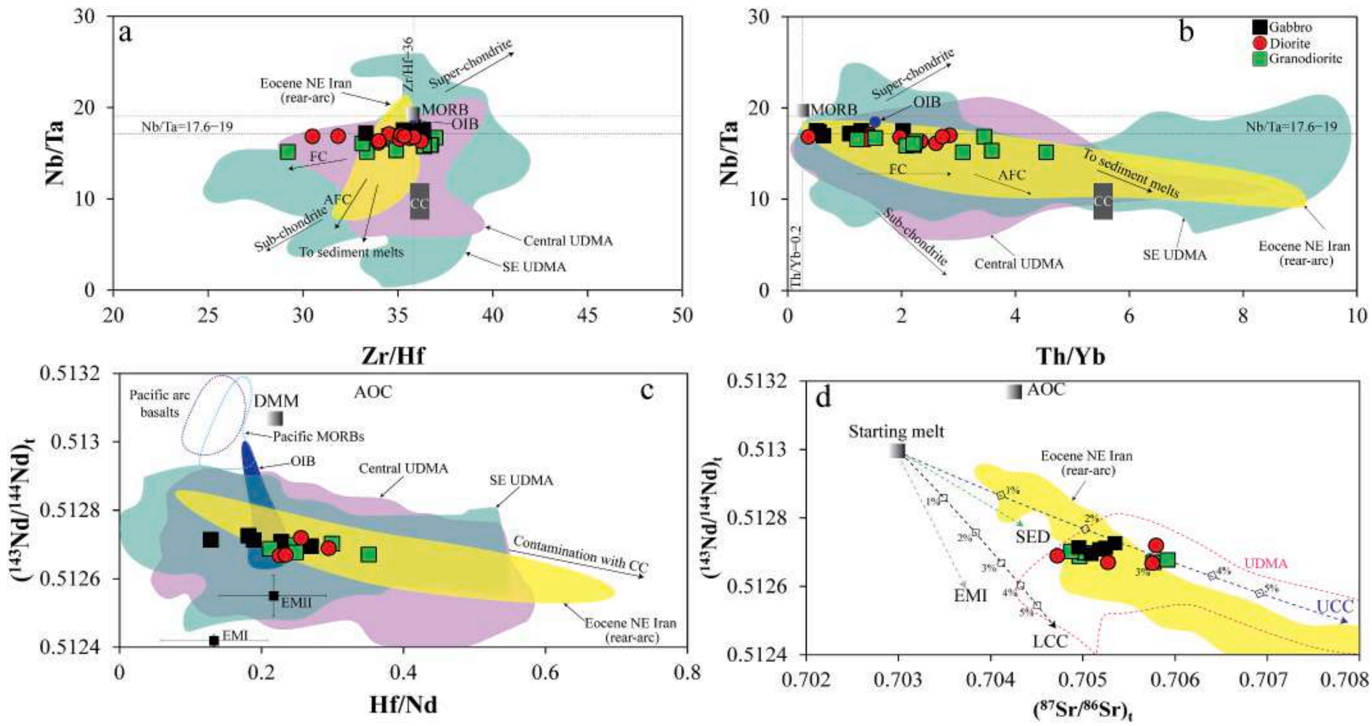

Fig. 10. (a and b) Plots of Nb/Ta *vs.* Zr/Hf and Th/Yb. (c and d) $^{143}Nd/^{144}Nd_{(t)}$ *vs.* Hf/Nd and $^{87}Sr/^{86}Sr_{(t)}$. The data dislocate toward the assimilation-fractional crystallization (AFC) trends, and modeled the contribution of no more than ~3% of Cadomian upper continental crustal (UCC) components in Kajan magma. The average Cadomian continental crust from Moghadam et al. (2015).

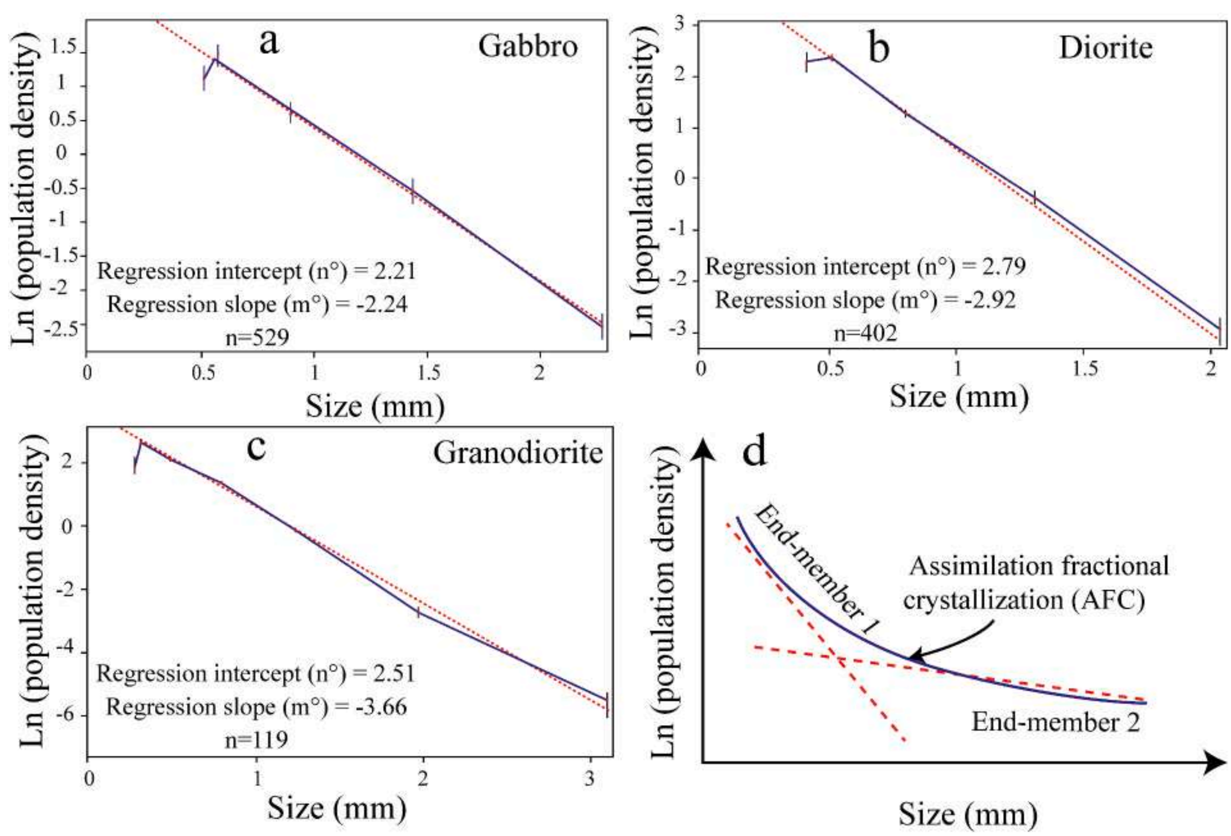

Fig. 11. (a–c) CSD plots of plagioclase crystals from Kajan plutonic rocks. Dotted lines are the regression lines calculated based on the frequency of crystal sizes, horizontal axis unit is in millimetres. The Kajan plots are almost parallel to the dotted lines (d) CSD patterns may change in response to physical processes in the magma chamber. Crustal contamination with different crystal density or coarse-grained crystals can result in concave-up CSD patterns (Higgins, 2006). The schematic patterns of processes that can influence the shape of the CSD are presented in Appendix Fig. 2.

6. Geodynamic implications

An approximately 95 Myr tectonic framework and evolutionary history of the UDMA encompasses magmatic "flare-up" and "lull" episodes (Appendix Fig. 3). Episodic magmatism is attributed globally to either tectonic events external to the arc (*e.g.,* change in subducting plate dip, age of the down-going slab, and convergence rate) or internal triggers (*e.g.,* underthrusting as a consequence of shortening in the retro-arc) (*e.g.,* DeCelles and Graham, 2015; Paterson and Ducea, 2015; Kirsch et al., 2016). The external forces during the ~95 Myr magmatism in the UDMA feasibly include: (i) close to flat-slab subduction during Paleocene and Early Eocene time as the plausible reason for the lull in magmatism (*e.g.,* Moghadam et al., 2020), and rapid trench migration followed by increase in down-going slab dip– corresponding to increase in volatile fluxing into mantle wedge– during Eocene onward (*e.g.,* Wortel and Spakman, 2000; Hafkenscheid et al., 2006), and (ii) systematic reduction in convergence velocities between Arabia and Eurasia (including Iran), *i.e.,* from ~6 cm/yr in Late Cretaceous, to ~4.5–5 cm/yr during flare-ups in Eocene (50–35 Ma), and ~ 3 cm/yr during Neogene (*c.f.,* Agard et al., 2007).

Our results suggest that the oldest yielded age (*i.e.,* 32 Ma) speaks against the following aspects of these tectonic models: (i) a lull in central UDMA magmatism from 37 to 26 Ma, and (ii) distinct flare-up magmatic episodes at ~54–37 Ma and ~ 20–5 Ma in the front arc, and ~ 45–40 Ma and ~ 30–25 Ma in the rear-arc as proposed by Sepidbar et al. (2019). Synthesizing our data with regionally appropriate values from the literature, we envision multistage tectono-magmatic events for this segment of the central UDMA, namely, Saveh to Nain regions (32° 30′ N to 36° 00′ N; ~ 500 km). Here, we find a plutonic mafic phase (~32 Ma) that is temporally distinct from the surrounding Zafarghand–Ardestan–Fesharak volcano–plutonic rocks exposed in the N–NW (~26.2–19.7 Ma; Yeganehfar et al., 2013; Babazadeh et al., 2017, 2019b; Kananian and Sarjoughian, 2017; Fig. 2), but younger than Kuh-e-Dom–Nasrand–Golshekanan–Soheyle-PaKuh granodiorites in the NE (~54–37 Ma; Sarjoughian and Kananian, 2017; Sarjoughian et al., 2019; Fig. 2) which are considered as *pre*-collisional products. The continuation of the Paleogene magmatism in the central UDMA proceeded with the presence of local mantle-dominant adakite-like magmatism (~18.5 Ma; Yeganehfar et al., 2013), and ended with *post*-collisional high-K magmatism during Middle to Late Miocene (~15–10 Ma; Babazadeh et al., 2019a, in review) following the collision between Arabian and Iranian plates. Thus, despite some mitigation in magmatic activity, we find no "lull" in magmatism for the central UDMA.

We are able also to address the mechanism of subduction in central to SE UDMA from Early Oligocene onward. A succession of studies has favored the initiation of slab break-off (and *post*-collisional magmatism) in Early Oligocene– Early Miocene time in the SE UDMA (*e.g.,* Omrani et al., 2008; Dargahi et al., 2010; Paul et al., 2010; Aghazadeh et al., 2015; Asadi, 2018; Nazarinia et al., 2020; Moghadam et al., 2022a, 2022b; Ghadami and Nazarinia, 2022; Yang et al., 2023) because there is no geophysical evidence for the subducted slab beneath the southeasternmost sector of the UDMA and west of the Makran today (*e.g.,* Stern et al., 2021; Moghadam et al., 2022a, 2022b), implying a slab-break-off at interval age of Early Oligocene– Early Miocene times. By contrast, subduction has been well described beneath the central segment of the UDMA (specifically 32° 30′ N to 36° 00′ N) from Oligocene to Early Miocene as confirmed by the presence of both calc-alkaline and slab-derived adakitic rocks (*e.g.,* Verdel et al., 2011; Yeganehfar et al., 2013; Chiu et al., 2013; Ghorbani et al., 2014; Babazadeh et al., 2017, 2019a, 2019b, 2023, 2024b; Raeisi et al., 2020, 2024; Khaksar et al., 2022).

We note that in terms of porphyry copper deposits (PCDs) the plutons studied here (*i.e.,* 32–22 Ma) are both non-adakitic and barren, in contrast to Middle Miocene Kahang plutons (*i.e.,* ~15 Ma; Babazadeh et al., in review) exposed ~1.5 km northwest of Kajan that are both non-adakitic and fertile. There is a general consensus that the transition from barren to fertile contexts in the UDMA was accompanied by change in crustal thickness and oxygen fugacity (fO_2) (*e.g.,* Zarasvandi et al., 2013; Rabiee et al., 2019, 2020, 2022; Khosravi et al., 2020, 2021; Raeisi et al., 2021, 2023, 2024). Interestingly, Moghadam et al. (2022b) invoke slab break-off and asthenospheric upwelling associated with Cu-bearing adakitic magmatism from Miocene onward in the SE UDMA. The same authors also suggest that a re-fertilized, hot and volatile-rich mantle might play a vital role on forming PCDs in this area.

Noting the presence of contemporaneous Cu-bearing non-adakitic- and adakitic rocks in central and SE UDMA, respectively, we corroborate the role of changes in the geometry and buoyancy of the subducting Neotethyan lithosphere (as per Moghadam et al., 2021a) and the responses of the overriding plate. We also propose somewhat different subduction mechanisms beneath central and SE UDMA from Oligocene onward. Taking into consideration the slab-derived adakitic magmatism in central UDMA, and no evidence for subducted slab beneath SE UDMA at Early Miocene time, we hypothesize tearing of the down-going slab into two spatially distinct shreds in the region between central and SE UDMA, and then buoyancy and change in the dip of subduction (as per Moghadam et al., 2021a) in the SE UDMA. We infer that the down-going slab was undergoing rollback beneath the central UDMA that facilitated ascending of lithospheric mantle melts at the same time whilst arc retreat was proceeding beneath the SE UDMA with detachment of subducted oceanic lithosphere (*i.e.,* slab break-off) and consequent influx of the hot asthenosphere (Fig. 12).

Synthesizing zircon $\varepsilon Hf_{(t)}$ and whole rock $\varepsilon Nd_{(t)}$ isotopic data of *pre*- to *post*-collisional settings (*e.g.,* Moghadam et al., 2022b) demonstrates that the products of the collision yielded higher values of $\varepsilon Hf_{(t)}$ and $\varepsilon Nd_{(t)}$ values. In this scenario, the Late Oligocene – Early Miocene magmatism of SE UDMA have significantly higher isotopic values of $\varepsilon Hf_{(t)}$ and $\varepsilon Nd_{(t)}$ (*i.e.,* $\varepsilon Hf_{(t)} = +1.8$ to $+14.9$ and $\varepsilon Nd_{(t)} = -1.5$ to $+5.3$) than their coeval in the central UDMA (*i.e.,* $\varepsilon Hf_{(t)} = -2.3.6$ to $+8.5$ and $\varepsilon Nd_{(t)} = -8$ to $+3.2$). Moghadam et al. (2022b) attributed higher $\varepsilon Hf_{(t)}$ values of the *post*-collisional magmatism to (*i*) paving of melt conduits to facilitate interaction between mantle-dominant melts and subordinate continental crust materials; (*ii*) interaction between mantle-derived melts and juvenile crust formed during the Eocene flare-up; and (*iii*) infiltration of magmas into the lower segments of continental crust to cannibalize previous intrusions with progressively less isotopic contrast due to dilution with mantle-derived magmas (*e.g.,* Storck et al., 2020). From a mineralization point of view, Raeisi et al. (2021) and Rabiee et al. (2022) by inference of geochemical and isotopic data proposed a progressive thickening of continental crust along with an increase in fO_2 following the collision between the Arabia and Iran plates as the plausible scenario for the formation of large fertile (*i.e.,* optimally productive) porphyry copper deposits (PCDs) throughout the UDMA from Oligocene–Miocene onward. The Tafresh, Natanz, and Niyasar granitoid rocks (20.1 Ma, 19.7 Ma, and 17.8 Ma, respectively; Raeisi et al., 2021; Babazadeh et al., 2024a; Honarmand et al., 2014, respectively) in central UDMA lack of the geochemical criteria for Cu-productivity (*i.e.,* barren). In contrast, SE UDMA granitoid rocks record optimally sub-productive to productive geochemical signatures during Oligocene to Early Miocene, *e.g.,* Bondar Hanza (~ 28 Ma; Mohebi et al., 2020), Zaftak ~28 Ma; Raeisi et al., 2021), Dali (~ 21–17 Ma; Aghazadeh et al., 2015), Chah-Firouzeh (~ 17 Ma; Mohammaddoost et al., 2017), Ali Abad (~ 16.5 Ma; Aghazadeh et al., 2015), and Darreh Zereshk (~ 16 Ma; Aghazadeh et al., 2015). In this scenario, the variable isotopic values in central- to SE UDMA at Late Oligocene – Early Miocene time, and the records of Cu-productivity pertaining to thickening of continental crust along with increasing fO_2, we hypothesize a diachronous collision in the central to SE UDMA, with priority in SE segments (Fig. 12). We infer that subduction in central UDMA also resulted ultimately in slab break-off (Babazadeh et al., in review) as proposed for the SE UDMA (Moghadam et al., 2022a, 2022b). However, the time of hard collision and detachment of subducted oceanic lithosphere might be spatially variable and likely did not coincide with processes taking place

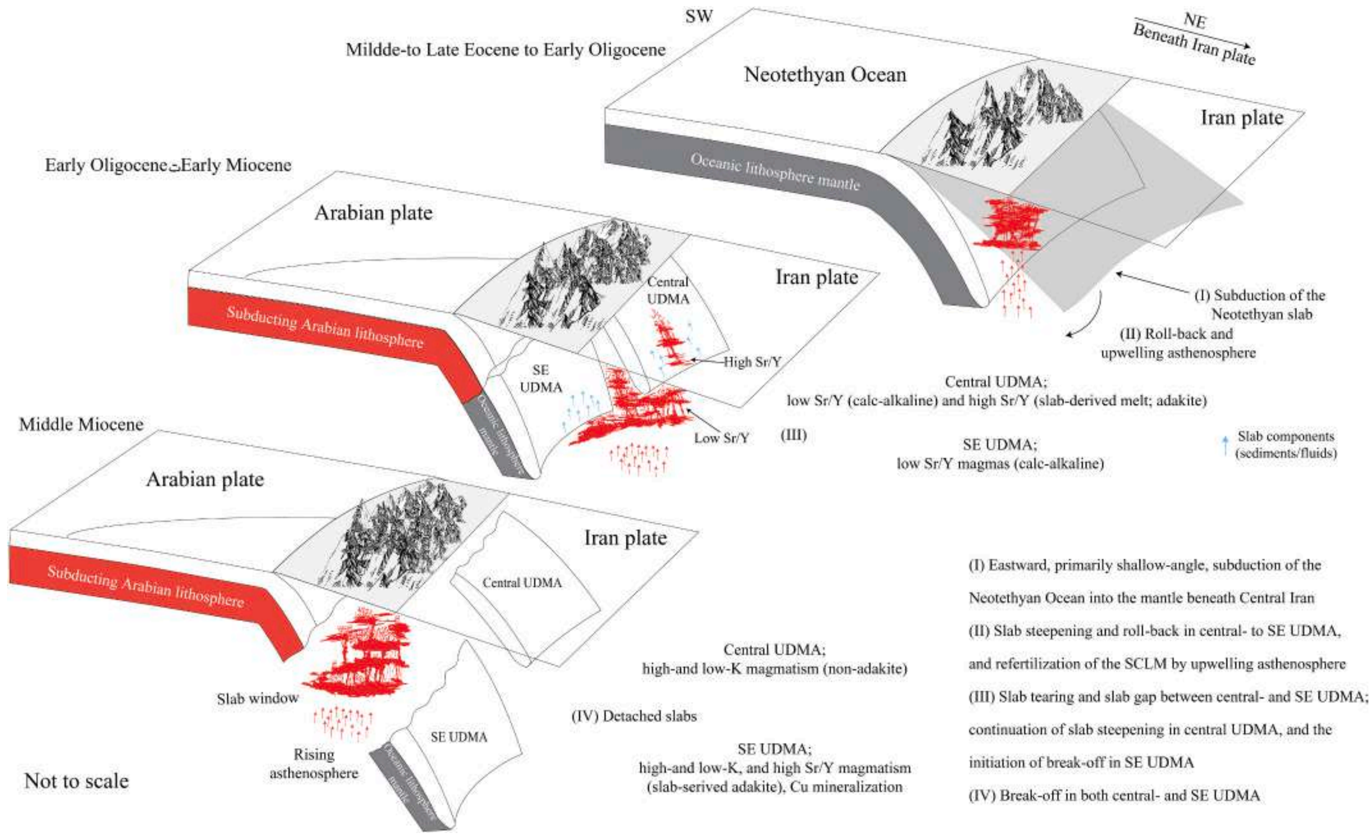

Fig. 12A. conceptual model for slab steepening and slab-tearing beneath the Central Iran plate during Middle Eocene to Middle Miocene. See text for further discussion.

in the SE segment of the UDMA. These findings bear important implications for the geodynamic evolution of the Zagros orogen and run counter to a model suggesting that the collision initiated in the northwest and propagated progressively to the southeast along the Zagros suture zone (*e.g.,* Chiu et al., 2013). The purported both slab steeping and slab tearing of the Neo-Tethys Ocean beneath Iran is not unique but analogous to Late Triassic–Early Jurassic tectonic setting of southwestern Gondwana (*e.g.,* Gianni et al., 2019), Late Triassic magmatism of eastern Tibet (*e.g.,* Chen et al., 2017), and within the western Hellenic subduction zone (*e.g.,* Hansen et al., 2019) where the geochemical and tomography data imply an intermittent evidence for the presence of a subducted slab.

7. Conclusion

Magmatic rocks in the Kajan region of the central UDMA have zircon U—Pb ages of 32 Ma to 22 Ma (*i.e.,* Early Oligocene to Early Miocene), reflecting a 10 My magmatic record. The rocks have $\varepsilon Nd_{(t)}$ from 1.18 to 2.25, zircon $\varepsilon Hf_{(t)}$ of −0.7 to +5.9, $^{206}Pb/^{204}Pb_{(t)} = 18.21$ to 18.36, $^{207}Pb/^{204}Pb_{(t)} = 15.48$ to 15.55, and $^{208}Pb/^{204}Pb_{(t)} = 37.91$ to 38.22. The geochemical and isotopic data are diagnostic of an active continental margin, and reflect melting of a metasomatized, enriched mantle. Mixing modeling of the samples indicate mixture of up to 97:3 of the batch mantle melt (*i.e.,* 98.5:1.5 of depleted mantle melt and terrigenous sediment): upper continental crust during magma evolution. The 32 Ma age of Kajan plutons is temporally distinct from the surrounding magmatic rocks, *i.e.*, ~54–37 Ma and ~ 26.2–20 Ma, and < 15 Ma, thus indicating no lull in central UDMA magmatism during the Cenozoic. The oldest age (32 Ma) further speaks against distinct flare-up magmatic episodes of ~54–37 Ma and ~ 20–5 Ma in the front arc. We hypothesize a plausible tearing of the down-going slab into two spatially separated shreds in the region between central and SE UDMA, with diachronous collision related to resulting changes in buoyancy and dip of subduction. The down-going slab was likely still involved in central UDMA (*i.e.,* rollback) whilst arc retreat beneath the SE UDMA proceeded with detachment of subducted oceanic lithosphere (*i.e.,* break-off). We hypothesize that the diachronous collision in the UDMA was initiated in SE segments of the UDMA, and then progressed into central UDMA. Despite the apparent difference in collision time, we suggest that subduction in central UDMA also ended with slab break-off similar to the SE UDMA.

Supplementary data to this article can be found online at https://doi.org/10.1016/j.chemgeo.2024.122247.

CRediT authorship contribution statement

Shahrouz Babazadeh: Writing – review & editing, Writing – original draft, Visualization, Software, Project administration, Methodology, Investigation, Funding acquisition, Conceptualization. **Davood Raeisi:** Writing – review & editing, Writing – original draft, Visualization, Software, Project administration, Methodology, Investigation, Funding acquisition, Conceptualization. **M. Santosh:** Writing – review & editing, Investigation, Funding acquisition, Formal analysis, Conceptualization. **Tanya Furman:** Writing – review & editing, Visualization, Funding acquisition, Formal analysis, Conceptualization. **Sung Hi Choi:** Writing – review & editing, Conceptualization. **Massimo D'Antonio:** Writing – review & editing, Visualization, Supervision, Project administration, Funding acquisition, Formal analysis, Conceptualization.

Declaration of competing interest

The authors declare that they have no known competing financial interests or personal relationships that could have appeared to influence the work reported in this paper.

Data availability

We have made our original data available in a data repository in Mendeley

The spatial–temporal evolution of Neotethyan subduction in central to southeast Iran: Constraints from geochemistry, zircon U–Pb–Hf, and Sr–Nd–Pb isotopes (Original data) (Mendeley Data)

Acknowledgements

S.B. expresses his gratitude to the DiSTAR–University Federico II of Naples, China University of Geosciences, and Penn State to all-out support of the scientific projects in Iran. S.B. and D.R. acknowledge for the contribution from 97007604 (Iran National Science Foundation; INSF) and 99.10871 (Iran Minerals Production and Supply Company; IMPASCO). The authors collectively express their own appreciation on M. Zhao, Y. An, and Z. Liu for their efforts in arrangements of data. We collectively express our gratitude to two anonymous reviewers whose comments have strengthened the paper, and to Dr. Sonja Aulbach for her excellent editorial handling.

References

Agard, P., Omrani, J., Jolivet, L., Mouthereau, F., 2005. Convergence history across Zagros (Iran): constraints from collisional and earlier deformation. Int. J. Earth Sci. 94, 401–419.

Agard, P., Omrani, J., Jolivet, L., Whitechurch, H., Vrielynck, B., Spakman, W., Monie, P., Meyer, B., Wortel, R., 2011. Zagros orogeny: a subduction-dominated process. Geol. Mag. 148, 692–725.

Aghazadeh, M., Hou, Z.Q., Badrzadeh, Z., Zhou, L.M., 2015. Temporal-spatial distribution and tectonic setting of porphyry copper deposits in Iran: constraints from zircon U–Pb and molybdenite Re–Os geochronology. Ore Geol. Rev. 70, 385–406.

Ahmadi, P., Ghorbani, M.R., Coltorti, M., Kuritani, T., Cai, Y., Fioretti, A.M., Braschi, E., Giacomoni, P.P., Aghabazaz, F., Babazadeh, S., Conticelli, S., 2019. High-Nb hawaiite-mugearite and high-Mg calc-alkaline lavas from northeastern Iran: Oligo–Miocene melts from modified mantle wedge. Int. Geol. Rev. 61, 150–174.

Alizadeh, E., Li, H., Babazadeh, S., Ma, C., Förster, M.W., 2023. Late Eocene slab retreat, extension, and mantle upwelling inferred from mantle signatures in potassium-rich magmatism in NE Iran. Int. Geol. Rev. 65 (9), 1586–1600.

Allen, M.B., Armstrong, H.A., 2008. Arabia–Eurasia collision and the forcing of mid-Cenozoic global cooling. Palaeogeogr. Palaeoclimatol. Palaeoecol. 265 (1–2), 52–58.

Annen, C., Blundy, J.D., 2008. Tracking the temperature of magmatic processes using mineral equilibria in granitoid rocks. J. Petrol. 49 (4), 861–891.

Annen, C., Sparks, R.S., 2002. Effects of repetitive emplacement of basaltic intrusions on thermal evolution and melt generation in the crust. Earth Planet. Sci. Lett. 203 (3–4), 937–955.

Ardill, K., Paterson, S., Memeti, V., 2018. Spatiotemporal magmatic focusing in upper–mid crustal plutons of the Sierra Nevada arc. Earth Planet. Sci. Lett. 498, 88–100.

Asadi, S., 2018. Triggers for the generation of post–collisional porphyry Cu systems in the Kerman magmatic copper belt, Iran: New constraints from elemental and isotopic (Sr–Nd–Hf–O) data. Gondwana Res. 64, 97–121.

Attia, S., Cottle, J.M., Paterson, S.R., 2020. Erupted zircon record of continental crust formation during mantle driven arc flare-ups. Geology 48, 446–451.

Azizi, H., Nouri, F., Stern, R.J., Azizi, M., Lucci, F., Asahara, Y., Zarinkoub, M.H., Chung, S.L., 2020. New evidence for Jurassic continental rifting in the northern Sanandaj Sirjan Zone, western Iran: the Ghalaylan seamount, southwest Ghorveh. Int. Geol. Rev. 62, 13–14.

Babazadeh, S., Mazaheri, S.A., Raghimi, M., Rahimi, A., 2014. Mineralogy, geochemistry and mass changes due to alteration of Khosh yeylagh volcanic rocks, East of Golestan province. Iranian J Crystall and Mineral 21 (4), 607–624 (in Persian with English abstract). http://ijcm.ir/article-1-267-fa.html.

Babazadeh, S., Ghorbani, M.R., Bröcker, M., D'Antonio, M., Cottle, J., Gebbing, T., Mazzeo, F.C., Ahmadi, P., 2017. Late Oligocene-Miocene mantle upwelling and interaction inferred from mantle signatures in gabbroic to granitic rocks from the Urumieh–Dokhtar arc, south Ardestan, Iran. Int. Geol. Rev. 59, 1590–1608.

Babazadeh, S., Ghorbani, M.R., Cottle, J.M., Bröcker, M., 2019a. Multi-stage tectono-magmatic evolution of the central Urumieh–Dokhtar magmatic arc, south Ardestan, Iran: Insights from zircon geochronology and geochemistry. Geol. J. 54 (4), 2447–247.

Babazadeh, S., Furman, T., Cottle, J.M., Raeisi, D., Lima, I., 2019b. Magma chamber evolution of the Ardestan pluton, Central Iran: evidence from mineral chemistry, zircon composition and crystal size distribution. Mineral. Mag. 83 (6), 763–780.

Babazadeh, S., Ghalamghash, J., Furman, T., D'Antonio, M., Raeisi, D., 2021a. The Oligocene Avaj volcanic – plutonic complex of Central Iran: a record of magma evolution and mineral–melt equilibria. J. Asian Earth Sci. 222, 104962.

Babazadeh, S., Ghalamghash, J., D`Antonio, M., Furman, T., 2021b. Hydrothermal alteration in Eshtehard volcanoes, Iran: Constraints from trace elements redistribution and stable isotope geochemistry. J. Geochem. Explor. 222, 106719.

Babazadeh, S., D`Antonio, M., Cottle, J.M., Ghalamghash, J., Raeisi, D., An, Y., 2021c. Constraints from geochemistry, zircon U–Pb geochronology and Hf–Nd isotopic compositions on the origin of Cenozoic volcanic rocks from central Urumieh–Dokhtar magmatic arc, Iran. Gondwana Res. 90, 27–46.

Babazadeh, S., Haase, K., Ghalamghash, J., Regelous, M., Poujol, M., Raeisi, D., Zhao, M., 2023. Magmatic evolution of the migrating central Urumieh–Dokhtar arc, Iran: Implications for magma production. Int. J. Earth Sci. 112 (5), 1577–1597.

Babazadeh, S., Ghalamghash, J., Raeisi, D., Santosh, M., Furman, T., Choi, S.H., D`Antonio, M., Heilimo, E., Cottle, J.M., 2024a. Arc magmatism associated with continental convergence in the SE segment of the UDMA, Iran: Insights from zircon geochronology and Hf–Sr–Nd–Fe isotopes. Lithos 466–467, 107468.

Babazadeh, S., D`Antonio, M., Raeisi, D., Furman, T., Santosh, M., Di Renzo, V., Klötzli, U., Choi, S.H., Ghalamghash, J., Cottle, J.M., Palin, R.M., 2024b. Geochemical and Sr–Nd–Hf isotopic evidence for Cenozoic partial melting of mantle beneath Natanz, Central Iran. Lithos 468–469, 107489.

Bachmann, O., Bergantz, G.W., 2004. On the origin of crystal-poor rhyolites: extracted from batholithic crystal mushes. J. Petrol. 45 (8), 1565–1582.

Bachmann, O., Bergantz, G.W., 2008. Rhyolites and their source mushes across tectonic settings. J. Petrol. 49 (12), 2277–2285.

Bindeman, I.N., Eiler, J.M., Yogodzinski, G.M., Tatsumi, Y., Stern, C.R., Grove, T.L., Portnyagin, M., Hoernle, K., Danyushevsky, L.V., 2005. Oxygen isotope evidence for slab melting in modem and ancient subduction zones. Earth Planet. Sci. Lett. 235, 480–496.

Burns, D.H., de Silva, S.L., Tepley III, F., Schmitt, A.K., Loewen, M.W., 2015. Recording the transition from flare-up to steady-state arc magmatism at the Purico–Chascon volcanic complex, northern Chile. Earth Planet. Sci. Lett. 422, 75–86.

Cashman, K.V., Blundy, J.D., 2000. Degassing and crystallization of ascending andesite and dacite. Philos. Trans. R. Soc. London, Ser. A 358 (1770), 1487–1513.

Cashman, K.V., Marsh, B.D., 1988. Crystal size distribution (CSD) in rocks and the kinetics and dynamics of crystallization II: Makaopuhi Lava Lake. Contrib. Mineral. Petrol. 99, 292–305.

Castillo, P.R., 2008. Origin of the adakite-high-Nb basalt association and its implications for post-subduction magmatism in Baja California, Mexico. Geol. Soc. Am. Bull. 120, 451–462.

Charlier, B.L., Wilson, C.J., Lowenstern, J.B., Blake, S., 2005. Magma generation at a large, hyperactive silicic volcano (Taupo, New Zealand) revealed by U–Th and U–Pb systematics in zircons. J. Petrol. 46 (1), 3–32.

Chekani Moghadam, M., Tahmasbi, Z., Ahmadi-Khalaji, A., Santos, J.F., 2018. Petrogenesis of Rabor-Lalehzar magmatic rocks (SE Iran): Constraints from whole rock chemistry and Sr-Nd isotopes. Chem. Erde 78, 58–77.

Chen, J.L., Xu, J.F., Ren, J.B., Huang, X.X., 2017. Late Triassic E-MORB-like basalts associated with porphyry Cu-deposits in the southern Yidun continental arc, eastern Tibet: Evidence of slab-tear during subduction? Ore Geology Reviews 90, 1054–1062.

Chiu, H.Y., Chung, S.L., Zarrinkoub, M.H., Mohammadi, S.S., Khatib, M.M., Lizuka, Y., 2013. Zircon U–Pb age constraints from Iran on the magmatic evolution related to Neotethyan subduction and Zagros orogeny. Lithos 162–163, 162–187.

Codillo, E.A., Le Roux, V., Marschall, H.R., 2018. Arc-like magmas generated by mélange-peridotite interaction in the mantle wedge. Nat. Commun. 9, 2864.

Dargahi, S., Arvin, M., Pan, Y., Babaei, A., 2010. Petrogenesis of post-collisional A-type granitoids from the Urumieh–Dokhtar magmatic assemblage, Southwestern Kerman, Iran: Constraints on the Arabian–Eurasian continental collision. Lithos 115 (1–4), 190–204.

De Celles, P.G., Ducea, M.N., Kapp, P., Zandt, G., 2009. Cyclicity in Cordilleran orogenic systems. Nature Geosci 2, 251–257.

DeCelles, P., Graham, S., 2015. Cyclical processes in the north American Cordilleran orogenic system. Geology 43, 499–502.

Decker, M., Schwartz, J., Stowell, H., Klepeis, K., Tulloch, A., Kitajima, K., Valley, J., Kylander-Clark, A., 2017. Slab-triggered arc flare-up in the cretaceous median Batholith and the growth of lower arc crust, Fiordland, New Zealand. J. Petrol. 58, 1145–1171.

Dokuz, A., Uysal, İ., Meisel, W., Turan, M., Duncan, R., Akcay, M., 2013. Post-collisional adakitic volcanism in the eastern part of the Sakarya zone, Turkey: evidence for slab and crustal melting. Contrib. Mineral. Petrol. 166, 1443–1468.

DePaolo, D.J., Daley, E.E., 2000. Neodymium isotopes in basalts of the southwest basin and range and lithospheric thinning during continental extension. Chemical Geology 169, 157–185.

Dokuz, A., Aydin, F., Karslı, O., 2019. Postcollisional transition from subduction- to intraplate-type magmatism in the eastern Sakarya zone, Turkey: Indicators of northern Neotethyan slab breakoff. GSA Bull. 131 (9–10), 1623–1642.

Du, W., Pei, L., Li, R., Li, Z., Liu, C., Wang, M., Lin, H., Pei, X., 2023. Zircon U–Pb dating and geochemical characteristics of Chahannuo gabbros in the northern margin of Qaidam basin, northern Tibetan plateau. Minerals 13, 651.

Ducea, M.N., Barton, M.D., 2007. Igniting flare-up events in Cordilleran arcs. Geology 35 (11), 1047–1050.

Ducea, M.N., Paterson, S.R., DeCelles, P.G., 2015. High-volume magmatic events in subduction systems. Elements 11 (2), 99–104.

Duggen, S., Portnyagin, M., Baker, J., Ulfbeck, D., Hoernle, K., Garbe-Schonberg, D., Grassineau, N., 2007. Drastic shift in lava geochemistry in the volcanic-front to reararc region of the Southern Kamchatkan subduction zone: evidence for the transition from slab surface dehydration to sediment melting. Geochim. Cosmochim. Acta 71, 452–480.

Ejima, T., Kon, Y., Kawano, S., Araoka, D., 2018. Zircon U–Pb dating of gabbro and diorite from the Bato pluton, northeast Japan. Island Arc 27, e12222.
Ekici, T., 2016. Collision-related slab break-off volcanism in the Eastern Anatolia, Kepez volcanic complex (Turkey). Geodin. Acta 28 (3), 223–239.
Elliott, T., 2003. Tracers of the slab. In: Eiler, J.M. (Ed.), Inside the Subduction Factory 11. American Geophysical Union, Washington, DC, pp. 23–45.
Eyuboglu, Y., Santosh, M., Yi, K., Bektaş, O., Kwon, S., 2012. Discovery of Miocene adakitic dacite from the Eastern Pontides Belt (NE Turkey) and a revised geodynamic model for the late Cenozoic evolution of the Eastern Mediterranean region. Lithos 146−147, 218–232.
Faccenna, C., Bellier, O., Martinod, J., Piromallo, C., Regard, V., 2006. Slab detachment beneath eastern Anatolia: A possible cause for the formation of the North Anatolian fault. Earth Planet. Sci. Lett. 242 (1–2), 85–97.
Fazlnia, A., Pang, K.N., Ji, W.Q., Pirouei, M., 2023. Geochemical constraints on Eocene ignimbrite flare-up in the Urumieh-Dokhtar magmatic arc, northwestern Iran. Lithos 450–451, 107189.
Fedele, L., Mehdipour Ghazi, J., Agostini, S., Ronca, S., Innocenzi, F., Lustrino, M., 2023. Concurrent adakitic and non-adakitic Late Miocene–Quaternary magmatism at the Sahand volcano, Urumieh–Dokhtar Magmatic Arc (NW Iran). Lithos 458–459, 107344.
Furman, T., Graham, D., 1999. Erosion of lithospheric mantle beneath the East African Rift system: Geochemical evidence from the Kivu volcanic province. Lithos 48, 237–262.
Ghadami, G., Nazarinia, A., 2022. Adakite signatures in granitoids northwest of Shahr-e-Babak, Kerman, Iran: constraints from geochemistry. N. Jb. Miner. Abh. (J. Min. Geochem.) 197 (3), 263–283.
Gianni, G.M., Navarrete, C., Spagnotto, S., 2019. Surface and mantle records reveal an ancient slab tear beneath Gondwana. Sci. Rep. 9 (1), 19774.
Golkaram, S., Rashidnejad-Omran, N., Azizi, H., Asahara, Y., Buchs, D.M., McDonald, I., Santos, J.F., 2016. Petrogenesis and geodynamic evolution of the Kajan Neogene subvolcanic rocks, Nain, Central Iran. Geochemistry 76 (4), 567–578.
Green, T.H., 1995. Significance of Nb/Ta as an indicator of geochemical processes in the crust–mantle system. Chem. Geol. 120, 347–359.
Griffin, W.L., Wang, X., Jackson, S.E., Pearson, N.J., O'Reilly, S.Y., Xu, X., Zhou, X., 2002. Zircons chemistry and magma genesis in SE China: in situ analysis of Hf isotopes, Pingtan and Tonglu igneous complexes. Lithos 61, 237–269.
Grosjean, M., Moritz, R., Rezeau, H., Hovakimyan, S., Ulianov, A., Chiaradia, M., Melkonyan, R., 2022. Arabia-Eurasia convergence and collision control on Cenozoic juvenile K-rich magmatism in the South Armenian block, Lesser Caucasus. Earth-Science Rev. 226, 103949.
Grove, T.L., Kinzler, R.J., 1986. Petrogenesis of andesites. Annu. Rev. Earth Planet. Sci. Lett. 14, 417–454.
Hafkenscheid, E., Wortel, M., Spakman, W., 2006. Subduction history of the Tethyan region derived from seismic tomography and tectonic reconstructions. J. Geophys. Res. Solid Earth 111.
Haghighi Bardineh, S.N., Zarei Sahamieh, R., Zamanian, H., Ahmadi Khalaji, A., 2018. Geochemical, Sr–Nd isotopic investigations and U–Pb zircon chronology of the Takht granodiorite, west Iran: Evidence for post-collisional magmatism in the northern part of the Urumieh-Dokhtar magmatic assemblage. J. Afr. Earth Sci. 139, 354–366.
Hansen, S.E., Evangelidis, C.P., Papadopoulos, G.A., 2019. Imaging slab detachment within the Western Hellenic subduction zone. Geochem. Geophys. Geosys. 20, 895–912.
He, J., Garzanti, E., Cao, L., Wang, H., 2020. The zircon story of the Pearl River (China) from Cretaceous to present. Earth Sci. Rev. 201, 103078.
Higgins, M.D., 2006. Quantitative Textural Measurements in Igneous and Metamorphic Petrology. Cambridge University Press.
Hofmann, A.W., 1997. Mantle geochemistry: the message from oceanic volcanism. Nature 385, 219–229.
Honarmand, M., Rashidnejad Omran, N., Neubauer, F., Emami, M.H., Nabatian, G., Liu, X., Dong, X., Dong, Y., Quadt, A., Chen, B., 2014. Laser-ICP-MS U–Pb zircon ages and geochemical and Sr–Nd–Pb isotopic compositions of the Niyasar plutonic complex, Iran: constraints on petrogenesis and tectonic evolution. Int. Geol. Rev. 56 (1), 104–132.
Honarmand, M., van der Boon, A., Neubauer, F., Heberer, B., Li, Q., Kuiper, K.F., Mason, P., Krijgsman, W., 2024. Geochemical constraints on the geodynamic setting of Alborz–Azerbaijan Cenozoic magmatism. Chem. Geol. 645 (5), 121889.
Hosseini, M.R., Hassanzadeh, J., Alirezaei, S., Sun, W., Li, C.Y., 2017. Age revision of the Neotethyan arc migration into the southeast Urumieh–Dokhtar belt of Iran: geochemistry and U–Pb zircon geochronology. Lithos 284, 296–309.
Huber, C., Bachmann, O., 2016. Fractional Crystallization: Insights from the Adamello Massif, Italian Alps. J. Petrol. 57 (3), 485–514.
İmer, A., Richards, J.P., Creaser, R.A., Spell, T.L., 2015. The late Oligocene Cevizlidere Cu−au− Mo deposit, Tunceli Province, eastern Turkey. Mineral. Deposita 50, 245–263.
Ionov, D.A., Griffin, W.L., O'Reilly, S.J., 1997. Volatile-bearing minerals and lithophile trace elements in the upper mantle. Chem. Geol. 141 (3–4), 153–184.
Javidi Moghadam, M., Karimpour, M.H., 2023. Eocene non-mineralization to Miocene porphyry copper mineralization-related magmatism in the Urumieh–Dokhtar magmatic arc, Iran. J. Geochem. Explor. 255, 107338.
Juricek, M.P., Keppler, H., 2023. Amphibole stability, water storage in the mantle, and the nature of the lithosphere-asthenosphere boundary. Earth Planet. Sci. Lett. 608, 118082.
Kaczmarek, M.A., Müntener, O., Rubatto, D., 2008. Trace element chemistry and U–Pb dating of zircons from oceanic gabbros and their relationship with whole rock composition (Lanzo, Italian Alps). Contrib. Mineral. Petrol. 155, 295–312.
Kananian, A., Sarjoughian, F., Nadimi, A., Ahmadian, J., Ling, W., 2014. Geochemical characteristics of the Kuh-e Dom intrusion, Urumieh–Dokhtar Magmatic Arc (Iran): Implications for source regions and magmatic evolution. J. Asian Earth Sci. 90, 137–148.
Kara, J., Väisänen, M., O'brien, H., 2022. Zircon dating of the basalt and felsic dyke in Haveri, SW Finland. Bull. Geol. Soc. Finl. 94, 109–118.
Karaoğlan, F., Parlak, O., Hejl, E., Neubauer, F., Klötzli, U., 2016. The temporal evolution of the active margin along the Southeast Anatolian Orogenic Belt (SE Turkey): Evidence from U–Pb, Ar–Ar and fission track chronology. Gondwana Res. 33, 190–208.
Karsli, O., Ketenci, M., Uysal, İ., Dokuz, A., Aydin, F., Chen, B., Wijbrans, J., 2011. Adakite-like granitoid porphyries in the Eastern Pontides, NE Turkey: potential parental melts and geodynamic implications. Lithos 127 (1–2), 354–372.
Karsli, O., Caran, Ş., Çoban, H., Şengün, F., Tekkanat, O., Andersen, T., 2020. Melting of the juvenile lower crust in a far-field response to roll-back of the southern Neotethyan oceanic lithosphere: the Oligocene adakitic dacites, NE Turkey. Lithos 370–371, 105614.
Kazemi, K., Kananian, A., Xiao, Y., Sarjoughian, F., 2019. Petrogenesis of middle-Eocene granitoids and their mafic microgranular enclaves in Central Urmia–Dokhtar Magmatic Arc (Iran): Evidence for interaction between felsic and mafic magmas. Geosci. Front. 10 (2), 705–723.
Kazemi, K., Kananian, A., Xiao, Y., Sarjoughian, F., 2020. Role of magma mixing in generating of the Gheshlagh–Aftabrow intrusions, SW Buin-Zahra, Iran: Evidence for a juvenile origin from geochemical and Sr−Nd isotopic data. Geol. J. 55 (1), 253–279.
Kazemi, K., Modabberi, S., Gharibnejad, P., Xiao, Y., Sarjoughian, F., Kananian, A., 2024. Mineral chemistry, trace elements, isotopic analysis, and zircon U-Pb dating in Hesar pluton, northern UDMA, Iran: implications for pre-collisional magma mixing. Acta Geologica Sinica-English Edition. https://doi.org/10.1111/1755-6724.15118.
Keskin, M., 2003. Magma generation by slab steepening and breakoff beneath a subduction-accretion complex: an alternative model for collision-related volcanism in Eastern Anatolia, Turkey. Geophys. Res. Lett. 30 (24), 8046.
Keskin, M., 2007. Eastern Anatolia: A hotspot in a collision zone without a mantle plume. In: Foulger, G.R., Jurdy, D.M. (Eds.), Plates, Plumes, and Planetary Processes, 430. Geological Society of America Special Paper, p. 693e722.
Keskin, M., Pearce, J.A., Mitchell, J., 1998. Volcano-stratigraphy and geochemistry of collision related volcanism on the Erzurum–Kars Plateau, northeastern Turkey. J. Volcanol. Geotherm. Res. 85, 355–404.
Khaksar, T., Rashidnejad-Omran, N., Li, S.Q., Song, S.Q., Kananian, A., Chen, F., Li, S., 2022. Geochronology and petrogenesis of granitoids and associated mafic enclaves from Ghohroud in the Urumieh–Dokhtar Magmatic Arc (Iran): Evidence for magma mixing during the closure of the Neotethyan Ocean. Geol. J. 57 (8), 3313–3332.
Khosravi, M., Rajabzadeh, M.A., Mernagh, T.P., Qin, K., Bagheri, H., Su, S., 2020. Origin of the ore-forming fluids of the Zefreh porphyry Cu–Mo prospect, Central Iran: constraints from fluid inclusions and sulfur isotopes. Ore Geol. Rev. 127, 103876.
Khosravi, M., Christiansen, E.H., Rajabzadeh, M.A., 2021. Chemistry of rock-forming silicate and sulfide minerals in the granitoids and volcanic rocks of the Zefreh porphyry Cu–Mo deposit, Central Iran: Implications for crystallization, alteration, and mineralization potential. Ore Geol. Rev. 134, 104150.
Kimura, J.I., Gill, J.B., Kunikiyo, T., Osaka, I., Shimoshioiri, Y., Katakuse, M., Kakubuchi, S., Nagao, T., Furuyama, K., Kamei, A., Nakajima, J., van Keken, P.E., Stern, R.J., 2014. Diverse Magmatic Effects of Subducting a Hot Slab in SW Japan: Results from Forward Modeling. Geoch. Geophys, Geosys, p. 15.
Kirsch, M., Paterson, S.R., Wobbe, F., Ardila, A.M.M., Clausen, B.L., Alasino, P.H., 2016. Temporal histories of Cordilleran continental arcs: testing models for magmatic episodicity. Am. Mineral. 101, 2133–2154.
Klaver, M., Djuly, T., de Graaf, S., Sakes, A., Wijbrans, J., Davies, G., Vroon, P., 2015. Temporal and spatial variations in provenance of Eastern Mediterranean Sea sediments: Implications for Aegean and Aeolian arc volcanism. Geochim. Cosmochim. Acta 153, 149–168.
Madanipour, S., Ehlers, T.A., Yassaghi, A., Rezaeian, M., Enkelmann, E., Bahroudi, A., 2013. Synchronous deformation on orogenic plateau margins: Insights from the Arabia-Eurasia collision. Tectonophysics 608, 440–451.
Lechmann, A., Burg, J.P., Ulmer, P., Guillong, M., Faridi, M., 2018. Metasomatized mantle as the source of Mid-MioceneQuaternary volcanism in NW-Iranian Azerbaijan: Geochronological and geochemical evidence. Lithos 304-307, 311–328.
Madanipour, S., Ehlers, T.A., Yassaghi, A., Enkelmann, E., 2017. Accelerated middle Miocene exhumation of the Talesh Mountains constrained by U–Th/He thermochronometry: evidence for the Arabia-Eurasia collision in the NW Iranian Plateau. Tectonics 36 (8), 1538–1561.
Marschall, H.R., Schumacher, J.C., 2012. Arc magmas sourced from mélange diapirs in subduction zones. Nat. Geosci. 5, 862–867.
Marsh, B.D., 1988. Crystal capture, sorting, and retention in convecting magma. J. Geophys. Res. Solid Earth 93 (B5), 4337–4350.
Martínez Ardila, A.M., Paterson, S.R., Memeti, V., Parada, M.A., Molina, P.G., 2019. Mantle driven cretaceous flare-ups in Cordilleran arcs. Lithos 326–327, 19–27.
Mazhari, N., Malekzadeh Shafaroudi, A., Ghaderi, M., Lackey, J.S., Farmer, G.L., Karimpour, M.H., 2017. Geochronological and geochemical characteristics of fractionated I-type granites associated with the skarn mineralization in the Sangan mining region NE Iran. Ore Geology Reviews 84, 116–133.
McQuarrie, N., van Hinsbergen, D.J.J., 2013. Retrodeforming the Arabia–Eurasia collision zone: age of collision versus magnitude of continental subduction. Geology 41, 315–318.
Middlemost, E.A.K., 1994. Naming materials in the magma/igneous rock system. Earth Sci. Rev. 37 (3–4), 215–224.

Moghadam, H.S., Khademi, M., Hu, Z.C., Stern, R.J., Santos, J.F., Wu, Y.B., 2015. Cadomian (Ediacaran–Cambrian) arc magmatism in the ChahJam–Biarjmand metamorphic complex (Iran): magmatism along the northern active margin of Gondwana. Gondwana Res. 27, 439–452.

Moghadam, H.S., Li, Q.L., Li, X.H., Stern, R.J., Levresse, G., Santos, J.F., Lopez Martinez, M., Ducea, M.N., Ghorbani, G., Hassannezhad, A., 2020. Neotethyan Subduction Ignited the Iran Arc and Back arc Differently. J. Geophys. Res. Solid Earth 125.

Moghadam, H.S., Griffin, W.L., Santos, J.F., Chen, R.X., Karsli, O., Lucci, F., Sepidbar, F., O'Reilly, S.Y., 2022a. Geochronology, geochemistry and petrology of the Oligocene magmatism in SE segment of the UDMB, Iran. Lithos 416–417, 106644.

Moghadam, H.S., Li, Q.L., Griffin, W.L., Stern, R.J., Santos, J.F., Ducea, M.N., Ottley, C. J., Karsli, O., Sepidbar, F., O'Reilly, S.Y., 2022b. Temporal changes in subduction- to collision-related magmatism in the Neotethyan orogen: the Southeast Iran example. Earth Sci. Rev. 226, 103930.

Moghadam, H.S., Li, Q.L., Li, X.H., Chiaradia, M., Karsli, O., Hoernle, K.A., Griffin, W.L., 2023. Mantle-derived high-K magmatic fluxes in northeast Iran arc: Constraints from zircon U–Pb–O–Hf and bulk rock major-trace elements and Sr–Nd–Pb isotopes. Gondwana Res. 119, 1–26.

Mohebi, A., Sepidbar, F., Mirnejad, H., Behzadi, M., 2020. Molybdenite Re-Os dating, petrology, and geochemistry of granitoids in the Bondar Hanza porphyry Cu deposit (Urumieh-Dokhtar magmatic arc), Iran: Insight into petrogenesis, mineralization, and tectonic setting. Geol. J. 55 (11), 7499–7516.

Moradi, S., Christiansen, E.H, Jiang, S.Y, Ghorbani, M.R., 2022. Petrogenesis and tectonic implications of Cenozoic mafic volcanic rocks in the Kahak area of central Urumieh−Dokhtar magmatic arc. Iran J. Asian Earth Sci. 239, 105404.

Moradi, S., Jiang, S.Y., Christiansen, E.H., Ghorbani, M.R., 2021. Petrogenesis of Tertiary granitoid rocks from east of the Bidhand fault, Urumieh–Dokhtar Magmatic Arc, Iran: Implication for an active continental margin setting. Lithos 400–401, 106422.

Morata, D., Oliva, C., de la Cruz, R., Suarez, M., 2005. The Bandurrias gabbro; late Oligocene alkaline magmatism in the Patagonian cordillera. J. S. Am. Earth Sci. 18, 147–162.

Moritz, R., Rezeau, H., Ovtcharova, M., Tayan, R., Melkonyan, R., Hovakimyan, S., Ramazanov, V., Selby, D., Ulianov, A., Chiaradia, M., Putlitz, B., 2016b. Long-lived, stationary magmatism and pulsed porphyry systems during Tethyan subduction to post-collision evolution in the southernmost Lesser Caucasus, Armenia and Nakhitchevan. Gondwana Res 37, 465–503.

Mouthereau, F., Lacombe, O., Verges, J., 2012. Building the Zagros collisional orogen: timing, strain distribution and the dynamics of Arabia/Eurasia plate convergence. Tectonophysics 532, 27–60.

Nayebi, N., Esmaeily, D., D'Antonio, M., Xia, X.P., Di Renzo, V., Lehmann, B., Shinjo, R., Babazadeh, S., Deevsalar, R., Modabberi, S., 2023. Zircon U–Pb ages and Sr–Nd–Pb–Hf isotopic compositions constrain the tectono-magmatic evolution of the Anomaly 21-A iron ore region, Bafq metallogenic province, Central Iran. J. Asian Earth Sci. 250, 105646.

Nayebi, N., Raeisi, D., Babazadeh, S., Xia, X.P., Santosh, M., 2024. Zircon U–Pb–Hf and whole rock Sr–Nd isotopic insights on the Silurian syenite–monzonite shoshonitic magmatism of Central Iran. Geol. J. 59 (2), 483–496.

Nazarinia, A., Mortazavi, M., Arvin, M., Hu, R., Zhao, C., Poosti, M., 2020. U–Pb zircon dating, Sr–Nd isotope and petrogenesis of Sarduiyeh granitoid in SE of the UDMA, Iran: implication for the source origin and magmatic evolution. Int. Geol. Rev. 62 (13–14), 1796–1814.

Nicollet, C., Paquette, J.L., Bruand, E., Bosse, V., Pereira, I., 2022. Crystallisation and fast cooling of the (meta) gabbro from the Chenaillet ophiolite (Western Alps): in-situ U-Pb dating of zircon, titanite, monazite and xenotime in textural context. Lithos 414−415, 106620.

Nielsen, S.G., Marschall, H.R., 2017. Geochemical evidence for melange melting in global arcs. Sci. Adv. 3 (4), e1602402.

Nouri, F., Azizi, H., Stern, R.J, Asahara, Y., Khodaparast, S., Madanipour, S., Yamamoto, K., 2018. Zircon U–Pb dating, geochemistry and evolution of the Late Eocene Saveh magmatic complex, central Iran: Partial melts of sub-continental lithospheric mantle and magmatic differentiation. Lithos 314–315, 274–292.

Nouri, F., Azizi, H., Asahari, Y., Stern, R., 2021. A new perspective on Cenozoic calc-alkaline and shoshonitic volcanic rocks, eastern Saveh (Central Iran). Int. Geol. Rev. 63 (4), 476–503.

Okay, A.İ., Zattin, M., Cavazza, W., 2010. Apatite fission-track data for the Miocene Arabia−Eurasia collision. Geology 38, 35–38.

Omidianfar, S., Monsef, I., Rahgoshay, M., Shafaii Moghadam, H., Cousens, B., Chen, M., Rajabpour, S., Zheng, J., 2022. Neo-Tethyan subduction triggered Eocene–Oligocene magmatism in eastern Iran. Geol. Mag. 160 (3), 490–510.

Omrani, J., Agard, P., Whitechurch, H., Benoit, M., Prouteau, G., Jolivet, L., 2008. Arc-magmatism and subduction history beneath the Zagros Mountains, Iran: a new report of adakites and geodynamic consequences. Lithos 106 (3–4), 380–398.

Pang, K.N., Chung, S.L., Zarrinkoub, M.H., Lin, Y.C., Lee, H.Y., Lo, C.H., Khatib, M.M., 2013. Iranian ultrapotassic volcanism at ~11 Ma signifies the initiation of post-collisional magmatism in the Arabia–Eurasia collision zone. Terra Nova 25, 405–413.

Paterson, S., Ducea, M., 2015. Arc Magmatic Tempos: Gathering the evidence. Elements 11, 91–97.

Paul, A., Hatzfeld, D., Kaviani, A., Tatar, M., Péquegnat, C., 2010. Seismic imaging of the lithospheric structure of the Zagros mountain belt (Iran). Geol. Soc. Spec. Publ. 330, 5–18.

Pearce, J.A., Peate, D.W., 1995. Tectonic Implications of the Composition of Volcanic Arc Magmas. Annu. Rev. Earth Planet. Sci. 23, 251–285.

Peccerillo, A, Taylor, S.R., 1976. Geochemistry of Eocene calc-alkaline volcanic rocks from the Kastamonu area, Northern Turkey. Contrib. Mineral. Petrol. 58, 63–81.

Putirka, K.D., 2008. Thermometers and barometers for volcanic systems. Rev. Mineral. Geochem. 69 (1), 61–120.

Rabayrol, F., Hart, C.J.R., Thorkelson, D.J., 2019. Temporal, spatial and geochemical evolution of late Cenozoic post-subduction magmatism in central and eastern Anatolia, Turkey. Lithos 336–337, 67–96.

Rabiee, A., Rossetti, F., Tecce, F., Asahara, Y., Azizi, H., Glodny, G., Lucci, F., Nozaem, R., Opitz, J., Selby, D., 2019. Multiphase magma intrusion, ore-enhancement and hydrothermal carbonatisation in the Siah-Kamar porphyry Mo deposit, Urumieh–Dokhtar magmatic zone, NW Iran. Ore Geol. Rev. 110, 102930.

Rabiee, A., Rossetti, F., Asahara, Y., Azizi, H., Lucci, F., Lustrino, M., Nozaem, R., 2020. Long-lived, Eocene-Miocene stationary magmatism in NW Iran along a transform plate boundary. Gondwana Res. 85, 237–262.

Rabiee, A., Rossetti, F., Lucci, F., Lustrino, M., 2022. Cenozoic porphyry and other hydrothermal ore deposits along the South Caucasus-West Iranian tectono-magmatic belt: a critical reappraisal of the controlling factors. Lithos 430–431, 106874.

Raeisi, D., Gholizade, K., Nayebi, N., Babazadeh, S., Nejadhadad, M., 2019. Geochemistry and mineral composition of lamprophyre dikes, Central Iran: implications for petrogenesis and mantle evolution. J. Earth Syst. Sci. 128, 74.

Raeisi, D., Mirnejad, H., McFarlane, C., Sheibi, M., Babazadeh, S., 2020. Geochemistry and zircon U–Pb geochronology of Miocene plutons in the Urumieh–Dokhtar magmatic arc, east Tafresh, Central Iran. Int. Geol. Rev. 62 (13–14), 1815–1827.

Raeisi, D., Zhao, M., Babazadeh, S., Long, L.E., Hajsadeghi, S., Modabberi, S., 2021. Synthesis on productive, sub productive and barren intrusions in the Urumieh–Dokhtar magmatic arc, Iran, constrains on geochronology and geochemistry. Ore Geol. Rev. 132, 103997.

Raeisi, D., Hajsadeghi, S., Hosseinzadehsabeti, E., Babazadeh, S., Lentz, D.R., Santosh, M., 2023. Exploration Targeting in the Shadan Porphyry Gold–Copper Deposit, Lut Block, Iran: Analysis of Spatial Distribution of Sheeted Veins and Lithogeochemical Data. Minerals 13 (4), 471.

Raeisi, D., Babazadeh, S., Long, L.E., Zhao, M., Cottle, J.M., Nayebi, N., Modabberi, S., 2024. Geochemical and isotopic signatures, and zircon U–Pb ages of the oldest known intrusive rocks associated with porphyry Cu deposits in the central Urumieh–Dokhtar magmatic arc, Iran. J. Geochem. Explor. 256, 107366.

Rezeau, H., Moritz, R., Wotzlaw, J.F., Tayan, R., Melkonyan, R., Ulianov, A., Selby, D., d'Abzac, F.X., Stern, R.A., 2016. Temporal and genetic link between incremental pluton assembly and pulsed porphyry Cu-Mo formation in accretionary orogens. Geology 44 (8), 627–630.

Rezeau, H., Moritz, R., Leuthold, J., Hovakimyan, S., Tayan, R., Chiaradia, M., 2017. 30 Myr of Cenozoic magmatism along the Tethyan margin during Arabia–Eurasia accretionary orogenesis (Meghri–Ordubad pluton, southernmost Lesser Caucasus). Lithos 288–289, 108–124.

Rezeau, H., Leuthold, J., Tayan, R., Hovakimyan, S., Ulianov, A., Kouzmanov, K., Moritz, R., 2018. Incremental growth of mid-to upper-crustal magma bodies during Arabia-Eurasia convergence and collision: a petrological study of the calc-alkaline to shoshonitic Meghri-Ordubad Pluton (Southern Armenia and Nakhitchevan, Lesser Caucasus). J. Petrol. 59 (5), 931–966.

Richards, J.P., Spell, T., Rameh, E., Razique, A., Fletcher, T., 2012. High Sr/Y magmas reflect arc maturity, high magmatic water content, and porphyry Cu ± Mo ± au potential: examples from the Tethyan arcs of central and eastern Iran and Western Pakistan. Econ. Geol. 107 (2), 295–332.

Rostami, M., Mazaheri, S.A., Mobasher, M., Babazadeh, S., Shorgeshty, M., 2014. Petrogenesis, Mineral Chemistry and Crystallization pressure and Temperature of Kuh-e Mish Granitoid from South Sheshtamad, Razavi-Khorasan Province. J Geochem 3 (2), 111–121.

Sarjoughian, F., Kananian, A., 2017. Zircon U–Pb geochronology and emplacement history of intrusive rocks in the Ardestan section, Central Iran. Geol. Acta 15 (1), 25–36.

Sarjoughian, F., Lentz, D., Kananian, A., Ao, S., Xiao, W., 2018. Geochemical and isotopic constraints on the role of juvenile crust and magma mixing in the UDMA magmatism, Iran: evidence from mafic microgranular enclaves and cogenetic granitoids in the Zafarghand igneous complex. Int. J. Earth Sci. 107, 1127–1151.

Sarjoughian, F., Azizi, M., Lentz, D.R., Ling, W., 2019. Geochemical and isotopic evidence for magma mixing/mingling in the Marshenan intrusion: Implications for juvenile crust in the Urumieh–Dokhtar Magmatic Arc, Central Iran. Geol. J. 54, 2241–2260.

Sarjoughian, F., Javadi, S., Azizi, H., Ling, W., Asahara, Y., Lentz, D.R., 2020. Geochemical and Sr–Nd isotopic constraints on the genesis of the Soheyle-PaKuh granitoid rocks (central Urumieh–Dokhtar magmatic belt, Iran). Int. Geol. Rev. 62, 1769–1795.

Sarjoughian, F., Lentz, D.R., Kazemi, K., Yousefi, F., 2022. Comparative analysis of exploration potential within the Urumieh Dokhtar Magmatic Arc, Iran, with a detailed example from mineral chemistry of the Marshenan intrusion. Chem. Geol. 594, 120767.

Schiano, P., Clocchiatti, R., Boivin, P., Medard, E., 2004. The nature of melt inclusions inside minerals in an ultramafic cumulate from Adak volcanic center, aleutian arc: implications for the origin of high-Al basalts. Chem. Geol. 203, 169–179.

Schildgen, T.F., Yıldırım, C., Cosentino, D., Strecker, M.R., 2014. Linking slab break-off, Hellenic trench retreat, and uplift of the Central and Eastern Anatolian plateaus. Earth Sci. Rev. 128, 147–168.

Schleiffarth, W., Darin, M., Reid, M., Umhoefer, P., 2018. Dynamics of episodic Late Cretaceous–Cenozoic magmatism across Central to Eastern Anatolia: New insights from an extensive geochronology compilation. Geosphere 14, 1–19.

Şengör, A.M.C., Özeren, M.S., Keskin, M., Sakınç, M., Özbakır, A.D., Kayan, I., 2008. Eastern Turkish high plateau as a small Turkic-type orogen: Implications for post-collisional crust forming processes in Turkic-type orogens. Earth Sci. Rev. 90, 1–48.

Sepahi, A.A., Nemati, B., Asiabanha, A., Lentz, D.R., McFarlane, C.R.M., 2023. New U-Pb zircon geochronological data for Takestan magmatic rocks (Western Alborz) and their significance for the interpretation of Paleogene magmatism in Iran. Int. Geol. Rev. https://doi.org/10.1080/00206814.2023.2291779.
Sepahvand, F., Tahmasebi, Z., Sarjoughian, F., Ebrahimi, M., Ling, W., Zhang, Z., Esmaeili, R., 2022. Juvenile crust and mantle sources for the Nasrand intrusive rocks, the central Urumieh–Dokhtar magmatic arc, Iran: Insights from elemental and isotopic geochemistry. Geol. J. 57 (7), 2608–2630.
Sepidbar, F., Ao, S., Palin, R.M., Li, Q.L., Zhang, Z., 2019. Origin, age and petrogenesis of barren (low-grade) granitoids from the Bzenjan–Bardsir magmatic complex, southeast of the Urumieh-Dokhtar magmatic belt, Iran. Ore Geol. Rev. 104, 132–147.
Shafiei, B., Haschke, M., Shahabpour, J., 2009. Recycling of orogenic arc crust triggers porphyry Cu mineralization in Kerman Cenozoic arc rocks, southeastern Iran. Miner. Deposita 44 (3), 265.
Shang, Z., Chen, Y., 2020. Zircon U−Pb geochronology, geochemistry and geological significance of the Anisian Alkaline Basalts in Gejiu District. Yunnan Province Miner. 10 (11), 1030.
Shao, T., Xia, Y., Ding, X., Cai, Y., Song, M., 2021. Zircon saturation in terrestrial basaltic melts and its geological implications. Solid Earth Sciences 4 (1), 27–42.
Sisson, T.W., Grove, T.L., 1993. Temperatures and H_2O contents of low-MgO high-alumina basalts. Contrib. Mineral. Petrol. 113, 167–184.
Stern, R.J., 2002. Subduction zones. Rev. Geophys. 40, 1012–1053.
Stern, R.J., Moghadam, H.S., Pirouz, M., Mooey, W., 2021. The Geodynamic Evolution of Iran. Annu. Rev. Earth Planet. Sci. 49, 9–36.
Stracke, A., Hofmann, A.W., Hart, S.R., 2005. FOZO, HIMU, and the rest of the mantle zoo. Geochem. Geophys. Geosyst. 6 (5), Q05007.
Sun, S.S., McDonough, W.F., 1989. Chemical and isotopic systematics of oceanic basalts: Implications for mantle composition and processes. In: Saunders, A.D., Norry, M.J. (Eds.), Magmatism in the Ocean Basins, Geological Society (London), vol. 42, pp. 313–345.
Tadayon, M., Rossetti, F., Zattin, M., Nozaem, R., Calzolari, G., Madanipour, S., Salvini, F., 2017. The Post-Eocene Evolution of the Doruneh Fault Region (Central Iran): the intraplate response to the reorganization of the Arabia-Eurasia collision Zone. Tectonics 36, 3038–3064.
Turner, S., Foden, J., 2001. U, Th and Ra disequilibria, Sr, Nd, and Pb isotope and trace element variations in Sunda arc lavas: predominance of a subducted sediment component. Contrib. Mineral. Petrol. 142, 43–57.
Turner, S.J., Langmuir, C.H., 2022a. Sediment and ocean crust both melt at subduction zones. Earth Planet. Sci. Lett. 584, 117424.
Turner, S.J., Langmuir, C.H., 2022b. An evaluation of five models of arc volcanism. J. Petrol. 63 (3), 1–25.
Verdel, C., Wernicke, B.P., Hassanzadeh, J., Guest, B., 2011. A Paleogene extensional arc flare-up in Iran. Tectonics 30 (3), 3008–3302.
Wang, M., Li, C., Xie, C.M., Xu, J.X., Li, X.K., 2015. U–Pb zircon age, geochemical and Lu–Hf isotopic constraints of the Southern Gangma Co basalts in the Central Qiangtang, northern Tibet. Tectonophysics 657, 219–229.
Wortel, M., Spakman, W., 2000. Subduction and slab detachment in the Mediterranean–Carpathian region. Science 290, 1910–1917.
Wu, Y., Qin, M.K., Zhang, C., Guo, G.L., Guo, D.F., Liu, F., Wu, W.W., Yang, J.S., 2022. SIMS zircon U-Pb ages and O isotope compositions of gabbro from the Laguoco ophiolite from western Shiquanhe–Yonzhu Suture Zone (Tibet) and their geological significance. Minerals 12, 1184.
Yang, G., Chen, L., Zhao, L.-F., Xie, X.-B., Yao, Z.-X., 2023. Crustal Lg attenuation beneath the Iranian Plateau: Implications for Cenozoic magmatism related to slab subduction, slab break-off, and mantle flow. J. Geophys. Res. Solid Earth 128 e2022JB025664.
Yeganehfar, H., Ghorbani, M.R., Shinjo, R., Ghaderi, M., 2013. Magmatic and geodynamic evolution of Urumieh–Dokhtar basic volcanism, Central Iran: Major, trace element, isotopic, and geochronologic implications. Int. Geol. Rev. 55 (6), 767–786.
Zarasvandi, A., Liaghat, S., Lentz, D., Hossaini, M., 2013. Characteristics of mineralizing fluids of the Darreh-Zerreshk and Ali-Abad Porphyry copper deposits, Central Iran, determined by fluid inclusion microthermometry. Resour. Geol. 63 (2), 188–209.
Zindler, A., Hart, S., 1986. Chemical geodynamics. Annu. Rev. Earth Planet. Sci. 14, 493–571.